

## Kinematics of HI Envelopes Associated with Molecular Clouds

THUMMIM MEKURIA<sup>1</sup> AND NIA IMARA<sup>1</sup><sup>1</sup>*Department of Astronomy and Astrophysics  
University of California, Santa Cruz CA, 95064, USA*

## ABSTRACT

We investigate the evolution of molecular clouds through the kinematics of their atomic hydrogen (HI) envelopes, using <sup>12</sup>CO and 21-cm emission to trace the molecular and atomic gas, respectively. We measure the large-scale gradients,  $\Omega$ , in the velocity fields of 22 molecular clouds and their HI envelopes, then calculate their specific angular momenta,  $j \propto \Omega R^2$ . The molecular clouds have a median velocity gradient of  $9.6 \times 10^{-2} \text{ km s}^{-1} \text{ pc}^{-1}$ , and a typical specific angular momentum of  $2.7 \times 10^{24} \text{ cm}^2 \text{ s}^{-1}$ . The HI envelopes have smaller velocity gradients than their respective molecular clouds, with an average of  $\Omega_{\text{HI}} = 0.03 \text{ km s}^{-1} \text{ pc}^{-1}$ , and a median angular momentum of  $j_{\text{HI}} \approx 5.7 \times 10^{24} \text{ cm}^2 \text{ s}^{-1}$ . For a majority of the systems,  $j_{\text{HI}} > j_{\text{H}_2}$ , with an average of  $j_{\text{HI}}/j_{\text{H}_2} = 4$ . Their velocity gradient directions tend to be misaligned, indicating that angular momentum is not conserved during molecular cloud formation. Both populations exhibit a  $j - R$  scaling consistent with that expected of supersonic turbulence:  $j_{\text{H}_2} \propto R^{1.67 \pm 0.22}$ , and  $j_{\text{HI}} \propto R^{1.71 \pm 0.27}$ . Combining our measurements with previous observations, we demonstrate a scaling of  $j \propto R^{1.50 \pm 0.02}$  in star-forming regions spanning 5 dex in size,  $R \in (10^{-3}, 10^2) \text{ pc}$ . We construct a model of angular momentum transport during molecular cloud formation, and derive the angular momenta of the progenitors to the present-day systems. We calculate a typical angular momentum redistribution timescale of 13 Myr, comparable to the HI envelope free-fall times.

## 1. INTRODUCTION

Large-scale linear velocity gradients are routinely observed across molecular clouds and cores (e.g., Kutner et al. 1977; Goodman et al. 1993; Rosolowsky et al. 2003; Imara & Blitz 2011; Imara et al. 2011; Tatematsu et al. 2016; Chen et al. 2019b; Braine et al. 2020). These gradients are often attributed to solid-body rotation, and used to infer the specific angular momentum,  $j \propto \Omega R^2$ , of these structures (e.g., Goodman et al. 1993; Tatematsu et al. 2016). The angular momentum of molecular clouds is of interest because it may have a significant impact on the outcomes of star-formation—e.g., the degree of fragmentation (Machida et al. 2008), the IMF (Shen et al. 2025), and proto-planetary disks sizes (Yen & Lee 2024).

Observations and theoretical studies agree that molecular clouds form when atomic hydrogen (HI) accumulates to surface densities exceeding  $10 M_{\odot} \text{ pc}^{-2}$ , sufficient to shield the H<sub>2</sub> molecule from dissociation by interstellar radiation (Krumholz et al. 2009; Imara & Burkhardt 2016; Sternberg et al. 2021; Park et al. 2023). Imara & Blitz (2011, hereafter IB) and Imara et al. (2011, hereafter IBB) were the first to compare the kinematics of the molecular and atomic phases of hydrogen

involved in the formation of molecular clouds. To do so, they devised a method for identifying the HI associated with molecular clouds using spatial and kinematic criteria. IB studied five star forming regions in the Solar Neighborhood, finding that the HI envelopes had an average velocity gradient of  $0.04 \text{ km s}^{-1} \text{ pc}^{-1}$ . The specific angular momenta they measured for the HI envelopes,  $j_{\text{HI}} \approx 1.9 \times 10^{25} \text{ cm}^2 \text{ s}^{-1}$ , were 2–5 times larger than the specific angular momenta of corresponding molecular clouds.

IBB identified the HI envelopes associated with 45 molecular clouds in M33 (Rosolowsky et al. 2003), and measured an average velocity gradient of  $\Omega_{\text{HI}} \approx 0.05 \text{ km s}^{-1} \text{ pc}^{-1}$ . They found that the HI envelopes had  $j_{\text{HI}} \approx 7.8 \times 10^{25} \text{ cm}^2 \text{ s}^{-1}$ , which is on average 27 times larger than the specific angular momentum of their corresponding molecular clouds. Both IB and IBB also found that the rotation axis of a molecular clouds and its HI envelope within a given system tend to be randomly oriented with respect to one another.

Had the molecular clouds formed by simple top-down collapse of atomic gas, the angular momentum of the HI would have been conserved in the molecular clouds. However, IB and IBB demonstrated that neither the magnitudes nor the orientation of the angular momenta

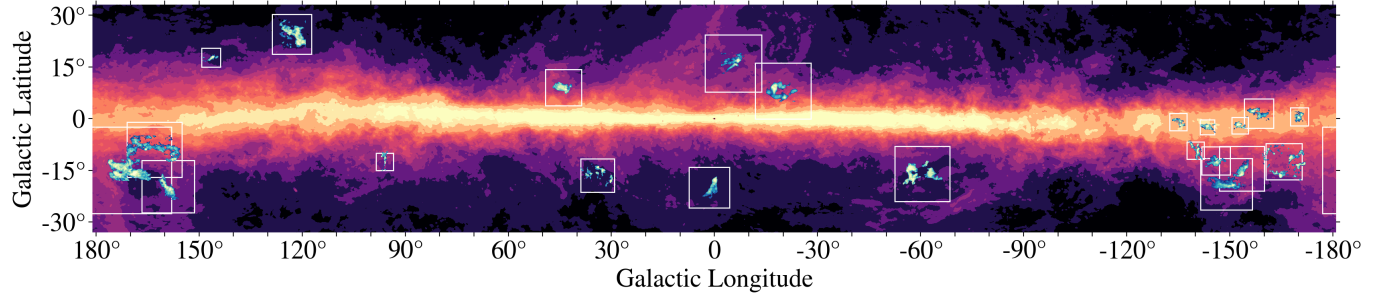


**Figure 1.** The Solar Neighborhood molecular clouds and their associated HI envelopes studied in this work (Table 1). The background map shows the surface density of HI with contours of  $\Sigma_{\text{HI}} \in (5 - 40) M_{\odot} \text{ pc}^{-2}$ , with an even spacing of  $5 M_{\odot} \text{ pc}^{-2}$ , as well as at  $[50, 75, 100] M_{\odot} \text{ pc}^{-2}$ . The white squares show the spatial extent of the HI envelope associated with each molecular cloud. (For ease of viewing, molecular gas not analyzed in this work is not included in the map.)

of the atomic and molecular gas are aligned. This so-called “angular momentum problem” is a long-standing puzzle (Larson 1981; Phillips 1999; Rosolowsky 2007; Imara et al. 2011), and has been attributed to gravitational (e.g., Larson 1984), magnetic (e.g., Mouschovias & Paleologou 1979; Misugi et al. 2024), and turbulent (e.g., Vázquez-Semadeni et al. 2024) torques braking molecular clouds during formation.

Furthermore, IBB measured the specific angular momenta of isolated HI clouds and found that they had lower rotational energies compared to their counterparts associated with molecular emission. The increased shear and rotational energy in the HI envelopes harboring molecular clouds suggests that the molecular clouds play a role in increasing the angular momentum of the HI in their vicinity. Magnetohydrodynamic simulations corroborate this view, demonstrating that molecular clouds dissipate angular momentum as they evolve (Arroyo-Chávez & Vázquez-Semadeni 2022; Misugi et al. 2024).

In this work, we investigate the kinematics of molecular clouds in the Solar Neighborhood to determine whether the findings presented by IB persist with higher resolution and higher sensitivity HI observations—which allow us to capture a larger dynamic range in density—and a sample of clouds that is  $\geq 4$  times larger. We go further than IB, exploring how specific angular momentum varies in star-forming regions over a wide range of evolutionary stages, and estimating the timescale for angular momentum redistribution during molecular cloud formation.

The paper is organized as follows: in Section 2, we present the catalog of molecular clouds we study and the observational data used to trace molecular and atomic hydrogen. Section 3 describes the spatial and kinematic criteria used to select the HI envelopes, as well as how we measure the physical properties of each population. Velocity field maps and kinematic properties of both populations are presented in Section 4. We quantify population level trends in Section 5, including a meta-analysis

of angular momentum measurements in the literature. In Section 6 we develop a physical model to follow angular momentum transport in the molecular and atomic phases, then contextualize our measurements within the large-scale motion of the Galaxy. We end with a summary in Section 7.

## 2. DATA

### 2.1. Molecular cloud sample

We select molecular clouds from the Zucker et al. (2019) catalog of dust-derived distances to Solar Neighborhood molecular clouds. Of the 27 regions targeted in Zucker et al. (2019), we exclude those located at extreme latitudes ( $|b| > 30^{\circ}$ ) or along lines of sight where the  $^{12}\text{CO}$  emission blends with the Galactic plane. The final sample (Table 1, Figure 1) consists of 22 molecular clouds, including the five in Imara & Blitz (2011), as well as other well-studied clouds such as  $\rho$ -Ophiuchus, the Polaris Flare, and Corona Australis.

### 2.2. $^{12}\text{CO}$ observations

The Dame, Hartmann, Thaddeus survey (Dame et al. 2001, hereafter DHT) is the most complete  $^{12}\text{CO}$  ( $J = 1 \rightarrow 0$ ) map of the Galaxy, capturing emission at latitudes  $\leq 30^{\circ}$  with an angular resolution of  $\theta = 8'.5$ . This corresponds to a linear resolution of 0.3 - 4 pc for the cloud distances in our catalog (150 - 2000 pc). The velocity resolution of the DHT is  $dv = 1.3 \text{ km s}^{-1}$ , and the data cover emission within  $|v| \leq 300 \text{ km s}^{-1}$  of the 115 GHz line center. Analyses are performed on the moment masked datacubes<sup>1</sup> (Dame 2011).

### 2.3. 21-cm observations

HI4PI (HI4PI Collaboration et al. 2016a) is the highest-sensitivity ( $\sigma_{\text{rms}} = 0.43 \text{ mK}$ ) and highest-

<sup>1</sup> DHT is available as position-position-velocity (ppv) datacubes at <https://lweb.cfa.harvard.edu/rtdc/CO>

resolution ( $\theta = 16'.2$ ) 21-cm map of the sky available to date. HI4PI outperforms the LAB survey (Kalberla et al. 2005), which IB used, by a factor of 8 in resolution. HI4PI covers emission within  $|v| \leq 600 \text{ km s}^{-1}$ , at a similar spectral resolution as DHT ( $1.29 \text{ km s}^{-1}$ ). We also resample the data onto a  $0.^{\circ}125$  grid to match the spatial resolution of DHT.<sup>2</sup> HI4PI is available as fits and HEALPix cubes in various projections (HI4PI Collaboration et al. 2016b); we use the fits cube in galactocentric coordinates, in cartesian projection for all subsequent analysis.

### 3. METHODOLOGY

Here we describe the spatial and kinematic criteria used to select the molecular clouds and their associated HI. We then present the physical properties of both populations and compare with previous findings.

#### 3.1. Identifying molecular clouds

The latitude and longitude ranges that we use to define the boundaries of the molecular clouds (Table 1) are guided by those given in Zucker et al. (2019). Given that  $^{12}\text{CO}$  becomes optically thick in molecular clouds at  $\text{H}_2$  column densities of  $\sim 10^{21} \text{ cm}^{-2}$  (Imara & Burkhart 2016), we use this threshold to define the lowest-level contour of the molecular clouds in the  $^{12}\text{CO}$  observations. For the majority of the clouds in our catalog, we mask data below  $N_{\text{H}_2} = 10^{21} \text{ cm}^{-2}$ . However, there are 9 smaller diffuse molecular clouds in our sample (Aquila South, Camelopardalis, Chamaeleon, Corona Australis, Crossbones, Hercules, Lacerta,  $\lambda$ -Orions, Polaris) with a significant fraction of their surface area containing emission below  $10^{21} \text{ cm}^{-2}$ ; for these we use a lower threshold of  $\log(N_{\text{H}_2}) = 20.5$ .

#### 3.2. Spatial and kinematic bounds of HI envelopes

Observations (e.g., Imara & Burkhart 2016; Park et al. 2023) show that molecular clouds in the Milky Way tend to be spatially and kinematically co-located with thick envelopes of atomic gas having surface densities of  $\geq 10 M_{\odot} \text{ pc}^{-2}$ . For a given molecular cloud, IB and IBB define its HI envelope as the atomic gas located inside a cylindrical volume, “the accumulation region,” centered on the cloud. The cylinder has a radius of  $R_{\text{HI}}$ , a height of  $2R_{\text{HI}}$ , and is oriented with its circular faces parallel to the midplane. Given that the scale height of HI is larger than  $\text{H}_2$ , the HI in the accumulation cylinder is expected to collapse along the z-axis when contracting (Blitz 1993; Rosolowsky et al. 2003; Imara & Blitz 2011).

<sup>2</sup> Measurements made using the resampled data are within a few percent of those made using the native resolution data.

The accumulation radius,  $R_{\text{HI}}$ , is set such that the mass of atomic hydrogen enclosed within the volume,  $M_{\text{HI}}$ , is at minimum equal to the molecular cloud mass,  $M_{\text{H}_2}$ .

We adopt the above definition and calculate the radius of an HI envelope as:

$$R_{\text{HI}} = \left( \frac{M_{\text{H}_2}}{2\pi n_{\text{HI}} \mu m_{\text{p}}} \right)^{1/3}, \quad (1)$$

where  $n_{\text{HI}}$  is the number density of atomic hydrogen,  $\mu$  is the mean molecular weight,  $m_{\text{p}}$  is the mass of a hydrogen atom, and  $M_{\text{H}_2}$  is the molecular cloud mass. We adopt a hydrogen number density of  $n_{\text{HI}} = 0.57 \text{ cm}^{-3}$ , a typical value for the warm neutral medium (Wolfire et al. 2003). The mean molecular weight is set for Solar metallicity:  $\mu = 1.36$ .

On sky, the accumulation region will appear as a square with a side length of  $2R_{\text{HI}}$ . To identify the atomic gas within this aperture that is kinematically associated with a given molecular cloud, we start by examining the velocity spectrum (Figure 2). We find that in all the systems, the emission peaks of the molecular cloud and its HI envelope spectra overlap with one another.

By fitting a Gaussian profile to each HI spectrum, we derive its line-center,  $\bar{v}_{\text{HI}}$ , and linewidth,  $\sigma_{\text{HI}}$ . We then define emission within  $\bar{v}_{\text{HI}} \pm 2\sigma_{\text{HI}}$  to be kinematically associated with the molecular cloud. The 21-cm spectra in the direction of some distant clouds (Canis Major OB1, Maddalena, Monoceros OB1, Rosette) consist of multiple emission peaks, likely due to blending with foreground HI. For these clouds, we constrain our selection of kinematically associated HI gas to velocity channels within  $\pm 1\sigma_{\text{HI}}$  of the 21-cm peak that lines up with the  $^{12}\text{CO}$  spectrum of the corresponding molecular cloud.

#### 3.3. Mass and radius

The mass of a molecular or atomic cloud is calculated as

$$M = \mu m_{\text{p}} \sum_{\text{pix}}^{N_{\text{pix}}} N_{\text{H}} \text{ d}A, \quad (2)$$

where  $N_{\text{H}}$  is the column density of hydrogen per pixel, and  $\text{d}A$  is the pixel area. The latter is equal to  $(d \text{ ds})^2$ , where  $d$  is the distance and  $ds$  is the pixel size. For a molecular cloud, the effective radius is determined from the total  $^{12}\text{CO}$  emitting area:  $R_{\text{H}_2} = \sqrt{(N_{\text{pix}} \text{ d}A)/\pi}$ .

The molecular clouds column density,  $N_{\text{H}_2}$ , is derived from the zeroth moment of the  $^{12}\text{CO}$  data:

$$N_{\text{H}_2} = X_{\text{CO}} \sum T_{\text{B}}(v) \text{ dv}, \quad (3)$$

**Table 1.** Location of molecular clouds and velocities of HI envelopes

Name	$l_0$	$l_1$	$b_0$	$b_1$	$d$	$\bar{v}_{\text{HI}}$	$\sigma_{v,\text{HI}}$
	deg	deg	deg	pc	km s <sup>-1</sup>		
Aquila South	41	29	-20	-12	$133 \pm 7.3$	1.9	2.5
California	171	155	-13	-2	$470 \pm 24.1$	-3.3	12.2
Camelopardalis	150	144	16	19	$213 \pm 13.6$	-0.5	3.3
Canis Major OB1	-132.5	-138.5	-2.5	1	$1209 \pm 60.1$	15.9	6.1
Chamaeleon	-54	-67	-20	-12	$183 \pm 9.5$	2.0	3.3
Corona Australis	4	-1	-24	-16	$151 \pm 8.5$	6.0	3.7
Crossbones	-138	-142	-12	-6.5	$886 \pm 44.2$	11.1	6.4
Gemini OB1	-164	-174	-3	3	$1786 \pm 89.1$	7.6	10.4
Hercules	49	41	7	11	$227 \pm 11.0$	5.3	5.1
Lacerta	98	94	-18	-8	$503 \pm 25.5$	0.1	5.3
Lupus	-14	-27	5	13	$189 \pm 12.7$	3.4	5.1
Maddalena	-140.5	-146.5	-5	-0.5	$2072 \pm 104.2$	24.7	11.4
Monoceros OB1	-155	-162	-0.5	3.5	$745 \pm 37.1$	8.8	7.3
Monoceros R2	-141	-149	-14.5	-10	$778 \pm 39.1$	8.7	6.1
Ophiuchus	0	-9	12	19	$144 \pm 7.3$	2.8	5.1
Orion A	-141	-155	-21	-16	$432 \pm 22.1$	7.1	6.3
Orion B	-149	-158	-17	-10	$423 \pm 21.1$	8.3	5.8
$\lambda$ -Orionis	-159.5	-173	-18	-7	$402 \pm 20.1$	6.6	7.3
Perseus	162	155	-26	-16	$294 \pm 15.1$	3.6	5.0
Polaris	127	118	20	30	$352 \pm 18.0$	-3.6	4.9
Rosette	-151	-155	-3.5	-0.5	$1304 \pm 65.2$	13.2	10.2
Taurus	177	164	-20	-11	$141 \pm 7.3$	5.0	6.1

Longitude ( $l$ ) and latitude ( $b$ ) and distances of the molecular clouds studied here, adapted from Zucker et al. (2019). The line-center ( $\bar{v}_{\text{HI}}$ ) and linewidth  $\sigma_{\text{HI}}$  are calculated by fitting a plane to the velocity spectrum of the HI envelope associated with each molecular cloud.

where  $X_{\text{CO}}$  is the metallicity-dependent CO-to-H<sub>2</sub> conversion factor,  $T_{\text{B}}$  is the brightness temperature, and  $dv$  is the velocity resolution. We adopt a value of  $X_{\text{CO}} = 1.97 \times 10^{20} \text{ cm}^{-2} (\text{K km s}^{-1})^{-1}$ , typical for solar metallicity gas (Lewis et al. 2022). The HI column density is calculated from the 21-cm emission, assuming the optically thin limit (Saha et al. 2018):

$$N_{\text{HI}} = 1.82 \times 10^{18} \sum T_{\text{B}}(v) \, dv \quad (4)$$

We list the masses and sizes of the molecular clouds and their atomic envelopes in Table 2. The molecular clouds have an average size of 17 pc, with the population spanning  $R_{\text{H}_2} \in (4, 43)$  pc. The HI accumulation radii are on average 2.8× larger, with a mean of 41 pc, and  $R_{\text{HI}}$  lying in the range (11, 83) pc. The molecular clouds cover a large range of masses:  $M_{\text{H}_2} \in (580, 2.7 \times 10^5) M_{\odot}$ , with an average of  $5.8 \times 10^4 M_{\odot}$  and a median of  $2.8 \times 10^4 M_{\odot}$ . The HI envelopes occupy a smaller range,  $M_{\text{HI}} \in (2.3 \times 10^3, 1.4 \times 10^6) M_{\odot}$ , with a mean of  $1.8 \times 10^5 M_{\odot}$  and median of  $8.1 \times 10^4 M_{\odot}$ .

On average, the HI masses measured from 21-cm emission are 8 times larger than the corresponding  $M_{\text{H}_2}$ . The latter was used as a lower limit to calculate the HI accumulation radius (Equation 1). A potential reason for this discrepancy could be that we underestimated the atomic hydrogen density when calculating  $R_{\text{HI}}$ . One could use the denser component of the neutral ISM, with  $n_{\text{CNM}} \sim 40 \times n_{\text{WNM}}$  (Wolfire et al. 2003), to trace the HI more directly associated with a molecular cloud. Since CNM is best traced in absorption (e.g., Sun et al. 2024; Stanimirović et al. 2014), surveys of HI self-absorption with comparable coverage and resolution to the <sup>12</sup>CO observations would be useful for such an analysis. A different reason could be that unrelated 21-cm emission along the line-of-sight is contributing to the integrated column density  $N_{\text{HI}}$  and thereby increasing the calculated HI envelope mass. Line-of-sight distance maps with comparable coverage and resolution to the <sup>12</sup>CO observations may be used to distinguish between the HI in the vicinity of the molecular cloud and unassociated atomic gas.

**Table 2.** Physical Properties of Molecular Clouds and their HI envelopes.

Name	$M_{\text{H}_2}$	$M_{\text{HI}}$	$R_{\text{H}_2}$	$R_{\text{HI}}$	$\Omega_{\text{H}_2}$	$\Omega_{\text{HI}}$	$\theta_{\text{H}_2}$	$\theta_{\text{HI}}$	$\rho_{\text{H}_2}$	$\rho_{\text{HI}}$	$j_{\text{H}_2}$	$j_{\text{HI}}$
	$10^4 M_{\odot}$		pc		$10^{-2} \text{ km s}^{-1} \text{ pc}^{-1}$		deg				$10^{24} \text{ cm}^2 \text{ s}^{-1}$	
AqS	0.07	0.23	$4.4 \pm 0.2$	$11.5 \pm 0.4$	$7.9 \pm 0.6$	$7.8 \pm 0.05$	108.0	118.0	0.76	0.99	$0.19 \pm 0.02$	$1.28 \pm 0.09$
Cal	14.37	41.19	$32.0 \pm 1.6$	$66.8 \pm 2.3$	$10.2 \pm 0.1$	$10.7 \pm 0.02$	-6.4	-74.1	0.99	0.99	$12.92 \pm 1.33$	$58.91 \pm 4.03$
Cam	0.06	0.24	$3.6 \pm 0.2$	$10.7 \pm 0.5$	$10.9 \pm 2.4$	$3.2 \pm 0.07$	-103.2	-80.2	0.53	0.77	$0.18 \pm 0.05$	$0.45 \pm 0.04$
CMO	7.97	14.83	$23.0 \pm 1.1$	$54.9 \pm 1.8$	$3.3 \pm 0.5$	$1.7 \pm 0.02$	-63.0	73.8	0.27	0.91	$2.19 \pm 0.38$	$6.47 \pm 0.44$
Chm	0.82	1.56	$9.2 \pm 0.5$	$25.7 \pm 0.9$	$10.5 \pm 0.2$	$2.8 \pm 0.02$	162.7	166.5	0.6	0.78	$1.08 \pm 0.11$	$2.30 \pm 0.16$
CrA	0.19	0.54	$5.0 \pm 0.3$	$15.8 \pm 0.6$	$8.8 \pm 0.6$	$1.1 \pm 0.04$	135.8	-166.4	0.62	0.4	$0.27 \pm 0.03$	$0.33 \pm 0.03$
Cbn	3.11	12.26	$22.6 \pm 1.1$	$40.1 \pm 1.3$	$5.8 \pm 0.2$	$5.4 \pm 0.05$	21.0	100.1	0.96	0.97	$3.64 \pm 0.38$	$10.62 \pm 0.71$
GmO	27.46	135.5	$38.3 \pm 1.9$	$82.9 \pm 2.8$	$6.0 \pm 0.3$	$3.2 \pm 0.02$	-38.3	-27.4	0.74	1.0	$10.79 \pm 1.22$	$27.52 \pm 1.84$
Her	0.46	1.68	$7.2 \pm 0.3$	$21.2 \pm 0.7$	$33.3 \pm 1.3$	$2.9 \pm 0.04$	-158.6	-90.3	0.66	0.81	$2.12 \pm 0.22$	$1.62 \pm 0.11$
Lac	0.56	2.03	$9.7 \pm 0.5$	$22.7 \pm 0.8$	$23.0 \pm 1.4$	$5.6 \pm 0.08$	26.1	106.7	0.93	0.97	$2.64 \pm 0.31$	$3.53 \pm 0.24$
Lup	0.98	4.06	$8.7 \pm 0.6$	$27.3 \pm 1.2$	$16.2 \pm 0.4$	$6.8 \pm 0.03$	97.3	80.8	0.82	0.81	$1.53 \pm 0.21$	$6.27 \pm 0.56$
Mad	22.0	58.5	$43.0 \pm 2.2$	$77.0 \pm 2.6$	$10.7 \pm 0.6$	$2.7 \pm 0.03$	75.2	95.4	0.74	0.95	$24.45 \pm 2.82$	$20.03 \pm 1.36$
MOB	8.35	16.58	$21.1 \pm 1.1$	$55.8 \pm 1.9$	$12.1 \pm 0.8$	$0.5 \pm 0.02$	92.6	-108.8	0.48	0.55	$6.64 \pm 0.79$	$2.01 \pm 0.15$
MR2	9.11	19.89	$23.3 \pm 1.2$	$57.4 \pm 1.9$	$6.4 \pm 0.2$	$3.1 \pm 0.02$	-153.5	97.3	0.93	0.94	$4.29 \pm 0.44$	$12.78 \pm 0.86$
Oph	0.44	1.94	$5.3 \pm 0.3$	$21 \pm 0.7$	$30.5 \pm 0.5$	$5.7 \pm 0.03$	-128.1	-70.1	0.76	0.96	$1.06 \pm 0.11$	$3.1 \pm 0.21$
OrA	9.01	16.34	$20.1 \pm 1.0$	$57.2 \pm 2.0$	$8.9 \pm 0.2$	$1.6 \pm 0.02$	-166.0	136.7	0.62	0.84	$4.44 \pm 0.47$	$6.49 \pm 0.45$
OrB	5.42	14.62	$13.2 \pm 0.7$	$48.3 \pm 1.6$	$0.9 \pm 0.4$	$2.2 \pm 0.03$	111.6	85.2	0.12	0.75	$0.20 \pm 0.09$	$6.24 \pm 0.42$
$\lambda$ Or	2.55	10.51	$18.5 \pm 0.9$	$37.6 \pm 1.2$	$20.6 \pm 0.3$	$2.9 \pm 0.02$	83.6	-0.9	0.64	0.96	$8.68 \pm 0.87$	$5.05 \pm 0.34$
Per	3.03	5.72	$11.5 \pm 0.6$	$39.8 \pm 1.4$	$23.9 \pm 0.5$	$3.7 \pm 0.03$	24.2	31.1	0.96	0.93	$3.92 \pm 0.41$	$7.23 \pm 0.50$
Pol	2.2	2.3	$18.6 \pm 1.0$	$35.7 \pm 31.2$	$6.7 \pm 0.2$	$2.4 \pm 0.02$	-4.2	22.0	0.76	0.91	$2.85 \pm 0.30$	$3.84 \pm 0.26$
Ros	8.86	3.023	$24.3 \pm 1.2$	$56.9 \pm 1.9$	$8.7 \pm 0.5$	$1.3 \pm 0.02$	-150.5	99.5	0.53	0.93	$6.31 \pm 0.74$	$5.36 \pm 0.37$
Tau	1.49	5.34	$9.7 \pm 0.5$	$31.4 \pm 1.1$	$8.4 \pm 0.2$	$8.2 \pm 0.03$	-119.2	-62.8	0.77	0.95	$0.97 \pm 0.1$	$9.90 \pm 0.68$

Notes: Physical properties calculated from  $^{12}\text{CO}$  and 21-cm observations. The properties listed include cloud mass ( $M$ ), radius ( $R$ ), velocity gradient magnitude ( $\Omega$ ) and direction ( $\theta$ ), Pearson coefficient ( $\rho$ ), and specific angular momentum ( $j$ ). The uncertainties in  $R$  are calculated from the distance uncertainties reported in (Zucker et al. 2019), and propagated to  $j$ . The latter is also dependent on the errors of the fit to Equation 6, which propagate through  $\Omega$ .

#### 4. VELOCITY GRADIENTS

Both molecular clouds and their associated HI envelopes are observed to have systematic, near-linear gradients in the velocity fields, often covering the whole extent of the cloud (e.g., Kutner et al. 1977; Goodman et al. 1993; Imara et al. 2011; Braine et al. 2018). In the following, we derive the velocity fields and calculate large-scale gradients of the molecular clouds and their atomic envelopes.

The velocity gradient  $\vec{\Omega}$  is measured from systematic variations in the first moment map, which maps the intensity-weighted centroid of emission at each pixel:

$$\langle v_{\text{LSR}} \rangle = \frac{\sum v T_{\text{B}}(v) \, dv}{\sum T_{\text{B}}(v) \, dv}, \quad (5)$$

We follow Goodman et al. (1993) and calculate  $\Omega$  by fitting a plane, given below, to the first moment maps.

$$v(x, y) = v_0 + \Omega_x(x - x_0) + \Omega_y(y - y_0), \quad (6)$$

Above,  $(x_0, y_0)$  is the center-of-mass (COM) of the cloud,  $v_0$  is velocity of the COM, and  $\Omega_x$  and  $\Omega_y$  are the gradient of  $\langle v_{\text{LSR}} \rangle$  along Galactic longitude and latitude, respectively.  $\Omega_x$ ,  $\Omega_y$ , and  $v_0$  and their respective uncertainties are obtained from a least-squares fit of Equation 6. The total magnitude and direction of the velocity gradient are calculated from these parameters as:

$$|\Omega| = \sqrt{\Omega_x^2 + \Omega_y^2} \quad (7)$$

$$\theta = \tan^{-1}(\Omega_y / \Omega_x). \quad (8)$$

$\theta$  is oriented such that the rotation axis of the cloud lies along  $\phi \equiv (\theta - 90^\circ)$ . In the rest of the text, we use the  $\vec{\Omega}$  to refer to the velocity gradient direction in vector form, and  $\Omega$  when referring to the magnitude.

##### 4.1. Results of gradient fitting

The magnitude and directions of the velocity gradients are listed in of Table 2. The molecular clouds have gradients in the range  $(0.09, 0.3) \text{ km s}^{-1} \text{ pc}^{-1}$ ,

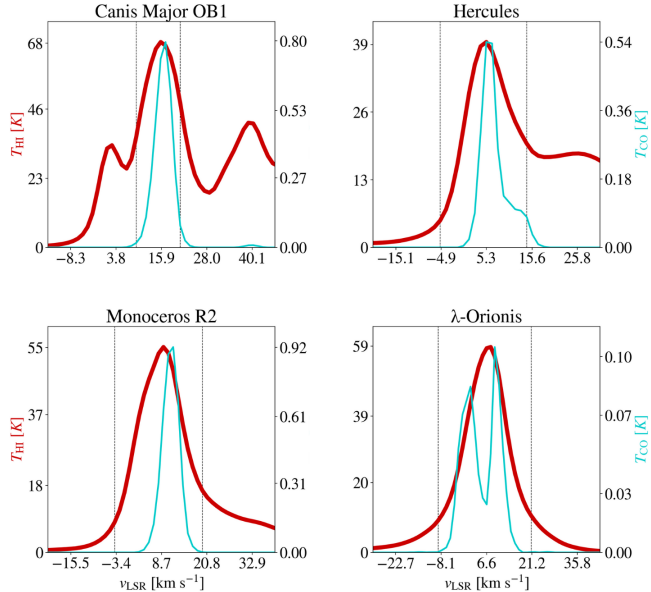


**Figure 2.** Velocity spectra of select molecular clouds (blue) and corresponding HI envelopes (red). The vertical lines indicate velocity bounds used to define the HI envelope. Spectra of the remaining molecular clouds and HI envelopes can be found in Appendix A.

with an average of  $\Omega_{\text{H}_2} = 0.12 \text{ km s}^{-1} \text{ pc}^{-1}$  and a median of  $0.96 \text{ km s}^{-1} \text{ pc}^{-1}$ . The HI envelopes have smaller velocity gradients than their molecular counterparts,  $\Omega_{\text{HI}} \in (0.005, 0.11) \text{ km s}^{-1} \text{ pc}^{-1}$ , with a typical value of  $0.03 \text{ km s}^{-1} \text{ pc}^{-1}$ . We do not find any correlation between  $\Omega_{\text{H}_2}$  and  $\Omega_{\text{HI}}$ .

If these velocity gradients arise due to solid body rotation, the typical rotational period of the molecular clouds is  $2\pi/\Omega_{\text{H}_2} \approx 65 \text{ Myr}$ ; an order of magnitude larger than both their median sound crossing time  $(R/\sigma)_{\text{H}_2} \approx 5.7 \text{ Myr}$  and median free-fall time  $t_{\text{ff},\text{H}_2} \approx 5.6 \text{ Myr}$ . The HI envelopes have similar crossing times to the molecular clouds,  $(R/\sigma)_{\text{H}_2} \approx 5.8 \text{ Myr}$  and longer free-fall times,  $t_{\text{ff},\text{HI}} \approx 13.8 \text{ Myr}$ . Due to their smaller gradients, the HI envelopes have longer periods,  $2\pi/\Omega_{\text{HI}} \approx 200 \text{ Myr}$ . In both populations, large-scale rotation is sub-dominant compared to turbulent and infall motions, although the discrepancy is decreased in the molecular clouds.

In Figure 4, we show the distribution of  $\Delta\theta \equiv |\theta_{\text{H}_2} - \theta_{\text{HI}}|$ , i.e., the separation between the rotation axes of molecular clouds and their HI envelopes. We find that 9 (40%) of the molecular clouds are co-rotating, i.e.,  $\Delta\theta < 45^\circ$ , with respect to their HI envelope. Similarly, Imara et al. (2011) find that less than half of the molecular clouds are co-rotating with respect to their HI envelopes.

#### 4.2. Goodness-of-fit of planar model

In a planar velocity field, the line-of-sight velocity,  $\langle v_{\text{LSR}} \rangle$ , will vary linearly with perpendicular distance from the rotation axis,  $\Delta r_\perp$ , with a slope equal to  $\Omega$ . To determine the extent to which the first moment maps of both populations clouds are planar, we plot the velocity profiles of both the molecular and atomic gas (Figure 5). For each velocity profile, we measure the Pearson correlation coefficient,  $\rho(\Delta r_\perp, \langle v_{\text{LSR}} \rangle)$ . The distribution of  $\rho$  for both populations is shown in Figure 6.

We find that 19 (86%) of the HI envelopes have velocity profiles with correlation coefficients  $\rho_{\text{HI}} \geq 0.75$ , of which 14 have  $\rho_{\text{HI}} > 0.9$ . Similarly, all but three of the molecular clouds have correlation coefficients greater than  $\rho_{\text{H}_2} \geq 0.5$ , and 10 have above 0.75. The molecular clouds have a median of  $\rho_{\text{H}_2} \approx 0.74$ , while the HI envelopes have a nearly linear median correlation coefficient of 0.94. This demonstrates that the velocity fields of both populations are reasonably well-approximated by a planar model, justifying the use of the large-scale 2D gradients to describe their kinematics.

#### 5. ANGULAR MOMENTUM

The angular momentum of a rotating body is given by:

$$\vec{J} = \vec{I} \times \vec{\omega} \approx cMR^2 \vec{\Omega}, \quad (9)$$

where the angular velocity,  $\omega$ , can be replaced by the velocity gradient,  $\Omega$ , for solid-body rotation ( $dv/dR = 0$ ), and  $c$  is an order-unity coefficient set by the body's shape, rotation axis, and density distribution. We adopt a value of  $c = 0.4$ , applicable to a uniform density sphere. For an object whose primary rotation axis is in the plane of the sky,  $\vec{\Omega}$  would appear as a linear gradient in the velocity field.

The rotational angular momentum per unit mass is then given by:

$$\vec{j} \equiv \frac{\vec{J}}{M} = cR^2 \vec{\Omega}. \quad (10)$$

Note that the large-scale gradient in the cloud velocity fields need not be due to rotation; Burkert & Bodenheimer (2000) have shown that a statistically robust distribution of the angular momenta of turbulent molecular clouds can be reproduced using the velocity gradient, as in the above equation. Below, we present our measurements of the specific angular momenta of the two phases,  $j_{\text{H}_2}$  and  $j_{\text{HI}}$ . We then discuss how  $j_{\text{H}_2}$  and  $j_{\text{HI}}$  compare with each other, as well as where they land among observations in the literature.

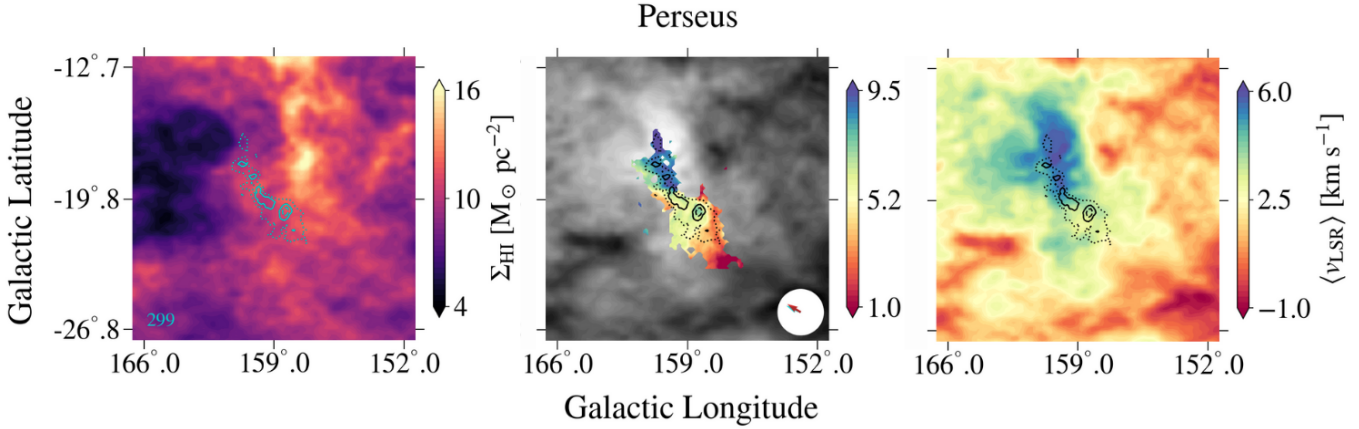


**Figure 3.** *Left:* Column density map of the HI envelope around the Perseus molecular cloud (black outline). The overlaid blue contours are at (0.25, 0.5, 0.75) times the peak H<sub>2</sub> surface density, which is indicated in lower left corner. *Middle:* Velocity field maps of the Perseus molecular cloud and *(right)* HI envelope, derived from the first moments of <sup>12</sup>CO and 21-cm emission at each pixel (Equation 5). The blue (red) arrow in the lower right corner of the middle panel indicates the velocity gradient direction  $\theta_{\text{H}_2}$  ( $\theta_{\text{HI}}$ ). Maps of the remaining molecular clouds and HI envelopes can be found in Appendix B.

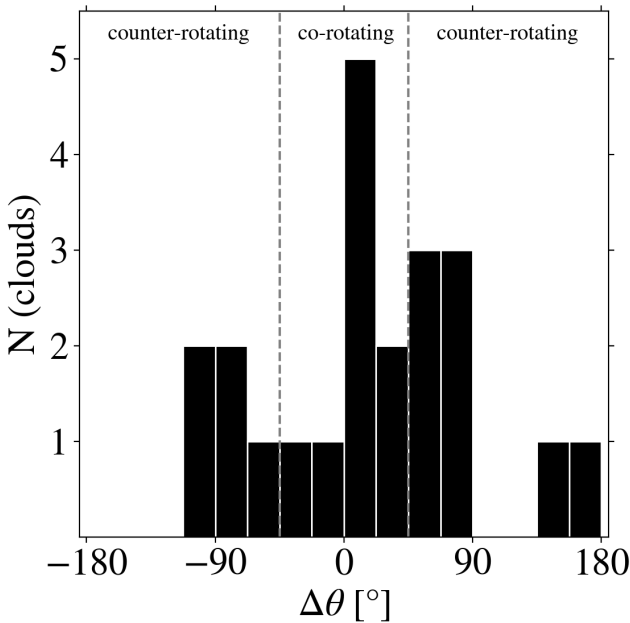


**Figure 4.** Distribution of angular separation between the rotation axis of molecular clouds and their corresponding HI envelopes.

### 5.1. Specific angular momentum

The molecular clouds have specific angular momenta in the range  $j_{\text{H}_2} \in (1.8 \times 10^{23}, 2.4 \times 10^{25}) \text{ cm}^2 \text{ s}^{-1}$ , with a median value of  $2.7 \times 10^{24} \text{ cm}^2 \text{ s}^{-1}$  (Table 2). On the other hand, the HI envelopes have  $j_{\text{HI}} \in (3.3 \times 10^{23}, 5.9 \times 10^{25}) \text{ cm}^2 \text{ s}^{-1}$ , with a median of  $5.8 \times 10^{24} \text{ cm}^2 \text{ s}^{-1}$ . We find that 17 of the systems have  $j_{\text{HI}}/j_{\text{H}_2} > 1$ , and the ratio of the specific angular momenta of the two phases spans 0.3–31, with an average of 4. This is similar to what IB measure for clouds in the

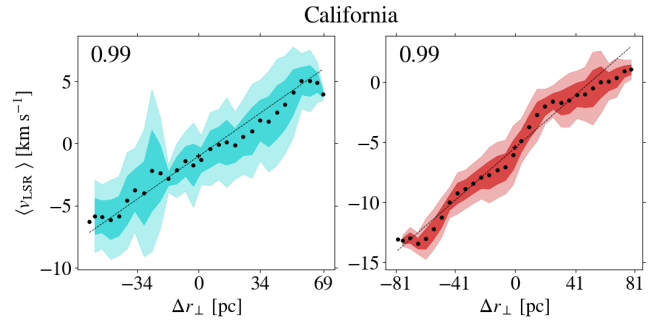


**Figure 5.** Intensity-weighted velocity centroid,  $\langle v_{\text{LSR}} \rangle$ , as a function of the perpendicular displacement,  $r_{\perp}$ , from the rotation axis of the California molecular cloud (*left*) and its HI envelope (*right*). The dashed lines indicate the planar model, and the shaded regions show the  $\pm 1\sigma$  and  $\pm 2\sigma$  scatter of the velocity field map at each radial bin. The Pearson correlation coefficient is in the upper left corner of each plot. Velocity profiles of the remaining molecular clouds and HI envelopes can be found available in the Appendix C.

Milky Way ( $j_{\text{HI}}/j_{\text{H}_2} \approx 3$ ) and about a factor of 7 smaller than what IB find for M33 clouds ( $j_{\text{HI}}/j_{\text{H}_2} \approx 27$ ). The HI specific angular momenta scale as  $j_{\text{HI}} \propto j_{\text{H}_2}^{0.62 \pm 0.12}$  (Figure 8), which is much steeper than the scaling IB determine in M33,  $j_{\text{HI}} \propto j_{\text{H}_2}^{-0.17 \pm 0.05}$ .

The angular momentum problem which IB demonstrated persists in the population level trends we find in this work. IB used masses calculated from the optically thick <sup>12</sup>CO line. For the velocity fields, they used <sup>13</sup>CO, since the narrower linewidth enables finer velocity resolution. For each of the five clouds in common—Perseus, Orion A, Mon OB1, Mon R2, and Rosette—we measure masses that are from  $\sim 1.3$  to 3.0 times higher than IB.

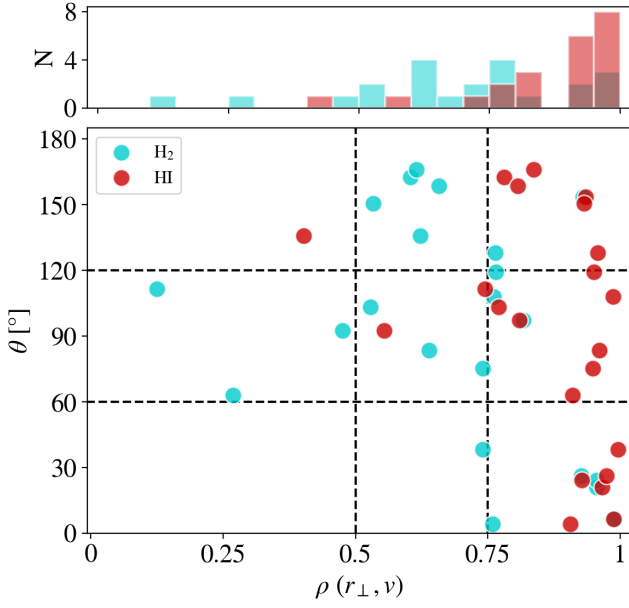


**Figure 6.** *Top:* Distribution of Pearson correlation coefficients for the molecular clouds (cyan) and the HI envelopes (red). *Below:* Velocity gradient directions as a function of Pearson coefficients. We observe highly linear gradients across all  $\theta_{\text{HI}}$ , while molecular clouds show a moderate correlation between larger  $\theta_{H_2}$  and smaller Pearson coefficients.

IB measure the large-scale velocity gradients of the molecular clouds using  $^{13}\text{CO}$ , while we use  $^{12}\text{CO}$  in this work. Our measurements for  $\Omega_{H_2}$  are consistent with one another for Monoceros R2, Perseus, and Rosette; on the other hand, we find that a nearly factor of 2 discrepancy for Monoceros OB1 and Orion A. The average  $j_{\text{HI}}/j_{H_2}$  we measure for the 5 clouds ( $\sim 1.5$ ) is smaller than the average ratio that we get for the whole population as well as what IB calculate. This is because the Monoceros OB1 and Rosette systems are part of the 4 pairs where  $j_{\text{HI}} < j_{H_2}$ .

The above results, combined with the mis-alignment between the angular momentum vectors of molecular clouds and their HI envelopes (Figure 4), argues that molecular cloud formation is more complicated than top-down, angular-momentum-conserving collapse of atomic gas. Instead, the observations suggest that angular momentum is redistributed as the molecular cloud forms. Alternatively, collapse may occur along multiple spatial dimensions simultaneously, and our model does not account for the third dimension into the plane of the sky—or mostly likely, a combination of both.

### 5.2. Scaling Relations

Turbulence plays a key role in supporting molecular clouds against gravitational collapse (e.g., Larson 1981). This turbulence is primarily supersonic, follow-

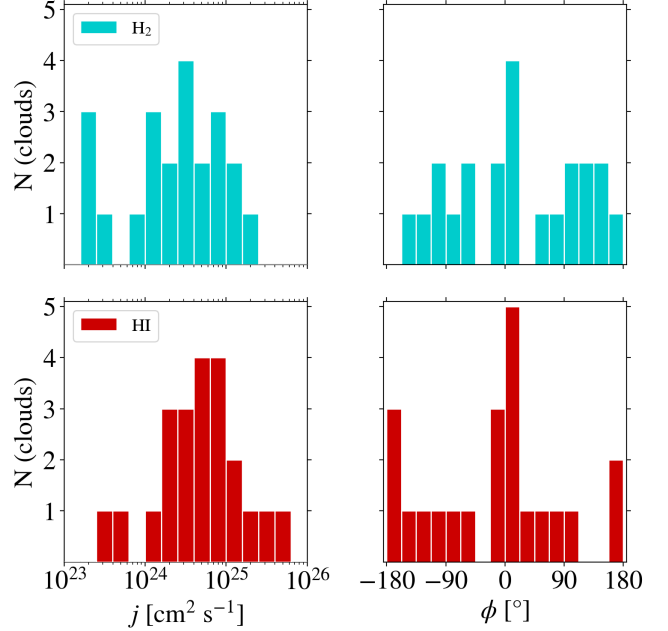


**Figure 7.** Kinematic properties of the molecular clouds (first row) and HI envelopes (second row). The magnitude and direction of the specific angular momenta of each population are shown in the left and right columns, respectively.

ing a size-linewidth scaling of  $\sigma \propto R^{1/2}$  (Burkert & Bodenheimer 2000). The angular velocity of a cloud and its linewidth scale as  $\Omega \propto \sigma/R$ , implying a specific angular momentum-size relation of  $j \propto R^{3/2}$  (Burkert & Bodenheimer 2000).

Least-squares fitting to our measurements shows that the molecular clouds have specific angular momenta that scale as  $j_{H_2} \propto R^{1.67 \pm 0.22}$ . The HI envelope follow a steeper scaling  $j_{\text{HI}} \propto R^{1.71 \pm 0.27}$ . Both are within  $1\sigma$  of the  $j \propto R^{1.5}$  relation expected of a supersonic turbulent cascade (Figure 9).

To examine the evolution of specific angular momentum across size scales—from the substructure in molecular clouds, to the atomic envelopes encompassing them—we combine our results with previous observations of the kinematics of star-forming regions. We draw from a database compiled by Phillips (1999) of observations of molecular clouds and cores spanning across three decades, utilizing a diversity of tracers (Phillips 1998). We also include recent observations conducted by Liu et al. (2021); Xu et al. (2020); Chen et al. (2019b); Punanova et al. (2018); Tatematsu et al. (2016); Yen et al. (2015); Imara et al. (2011); Tobin et al. (2011); Chen et al. (2007); Pirogov et al. (2003); Caselli et al. (2002). Similar meta-analyses have been done in the past for observational (e.g., Pandhi et al. 2023; Chen et al. 2019a; Phillips 1999) and simulated cloud populations (e.g., Arroyo-Chavez et al. 2026; Chen & Ostriker

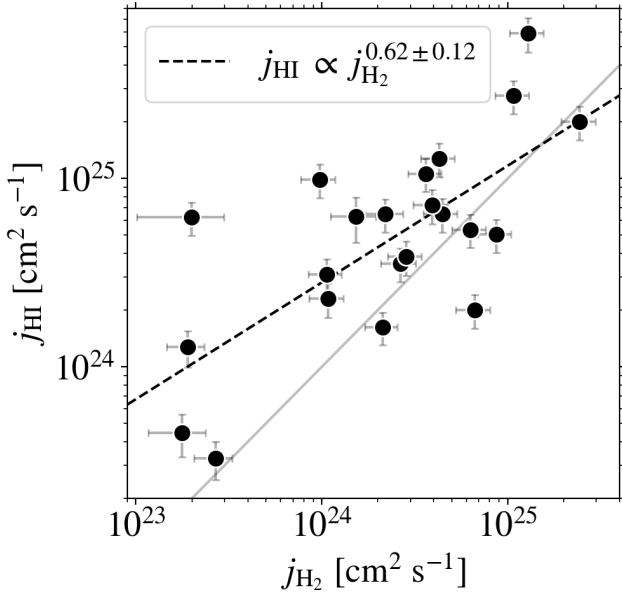


**Figure 8.** The specific angular momentum of HI envelopes with respect to those of their corresponding molecular clouds. The error bars are indicate the  $1-\sigma$  uncertainty of each measurement, derived from the distance uncertainties reported in (Zucker et al. 2019) and the errors of fitting a plane to the first moment maps, reported in Table 2. The grey solid indicates where  $j_{\text{HI}} = j_{\text{H}_2}$ , and the black dashed line is the least-squares best fit to the data.

2018). In this work we combine for the first time observational data over 5 orders of magnitude in size, including extragalactic clouds. To facilitate comparison, we calculate all specific angular momenta using the geometric coefficient of 0.4, even when the original work does otherwise. Where there is a major and minor axis reported for the spatial extent of an object, we calculate the radius as the geometric mean of the two.

With the results from this study, we show that molecular clouds and cores in the size range  $R \in (10^{-3}, 10^2)$  pc follow a power-law relationship of  $j \propto R^{1.50 \pm 0.02}$  (Figure 10). This suggests that angular momentum evolves uniformly with size throughout the ISM from dense pre-stellar cores to diffuse atomic clouds.

## 6. DISCUSSION

We now describe a simple physical model describing angular momentum transport that occurs during the formation of a molecular cloud. We calculate the properties of the progenitor atomic gas from which a molecular cloud forms. We also calculate the timescale for angular momentum redistribution and analyze the motion of HI envelopes within the context of the Galaxy.

### 6.1. Estimating momentum transport timescales

Magnetohydrodynamic simulations (e.g., Misugi et al. 2024; Arroyo-Chávez & Vázquez-Semadeni 2022) demonstrate that molecular clouds lose angular momentum over time as they form. Arroyo-Chávez & Vázquez-Semadeni (2022) find that as the gas undergoes hierarchical gravitational collapse, angular momentum is transported from the dense, contracting molecular cloud into the surrounding diffuse atomic gas. Below, we describe the molecular cloud and HI envelope as a co-evolving system with a shared common progenitor, in order to estimate the timescale for angular momentum transport in molecular clouds.

Let us imagine a progenitor HI cloud with initial angular momentum  $J_{\text{init}}$  that, due to gravitational collapse or shocks, increases in density sufficiently to form a molecular cloud in its interior. The present-day HI we observe will be the gas that remained atomic and has co-evolved with the molecular cloud. The total angular momentum of this system would be:

$$\overrightarrow{J}_{\text{total}} = \overrightarrow{J}_{\text{init}} + \overrightarrow{J} = (\overrightarrow{J}_{\text{HI}} + \overrightarrow{J}_{\text{H}_2})_{\text{present}} \quad (11)$$

where  $J_{\text{HI}}$  and  $J_{\text{H}_2}$  are the total angular momenta of the present HI envelope and molecular cloud respectively,  $J_{\text{init}}$  is the total angular momentum of the progenitor, and  $\overrightarrow{J}$  is the change in angular momentum due to interactions with the environment, e.g., inflowing or outflowing gas. In the simplest scenario of an isolated system,  $\overrightarrow{J} = 0$  and  $M_{\text{tot}} = M_{\text{init}} = M_{\text{HI}} + M_{\text{H}_2}$ . The specific angular momentum of the progenitor HI cloud can then be written as:

$$M_{\text{H}_2} \overrightarrow{j}_{\text{H}_2} + M_{\text{HI}} \overrightarrow{j}_{\text{HI}} = M_{\text{tot}} \overrightarrow{j}_{\text{init}} \quad (12)$$

Writing out the components of the vectors explicitly, we get:

$$\frac{c}{M_{\text{tot}}} \sum M_h R_h^2 \begin{pmatrix} \Omega_x \\ \Omega_y \end{pmatrix}_h = \begin{pmatrix} j_x \\ j_y \end{pmatrix}_{\text{init}}. \quad (13)$$

where the index  $h$  in the sum goes over the molecular cloud and HI envelope, and we have assumed that both cloud phases are described by the same geometric factor  $c$ . While the total angular momentum is a 3-dimensional vector, we restrict our calculations to the two on-sky components,  $x$  and  $y$ , accessible from observations.

The progenitor HI clouds of the systems we study here have angular momenta of  $j_{\text{init}} \in (2.8 \times 10^{23}, 4.5 \times 10^{25}) \text{ cm}^2 \text{ s}^{-1}$ , with a median of  $4.2 \times 10^{24} \text{ cm}^2 \text{ s}^{-1}$ . The progenitor clouds have specific angular momenta that are  $\approx 3$  times larger than  $j_{\text{H}_2}$  and  $0.8 \times j_{\text{HI}}$ , which puts

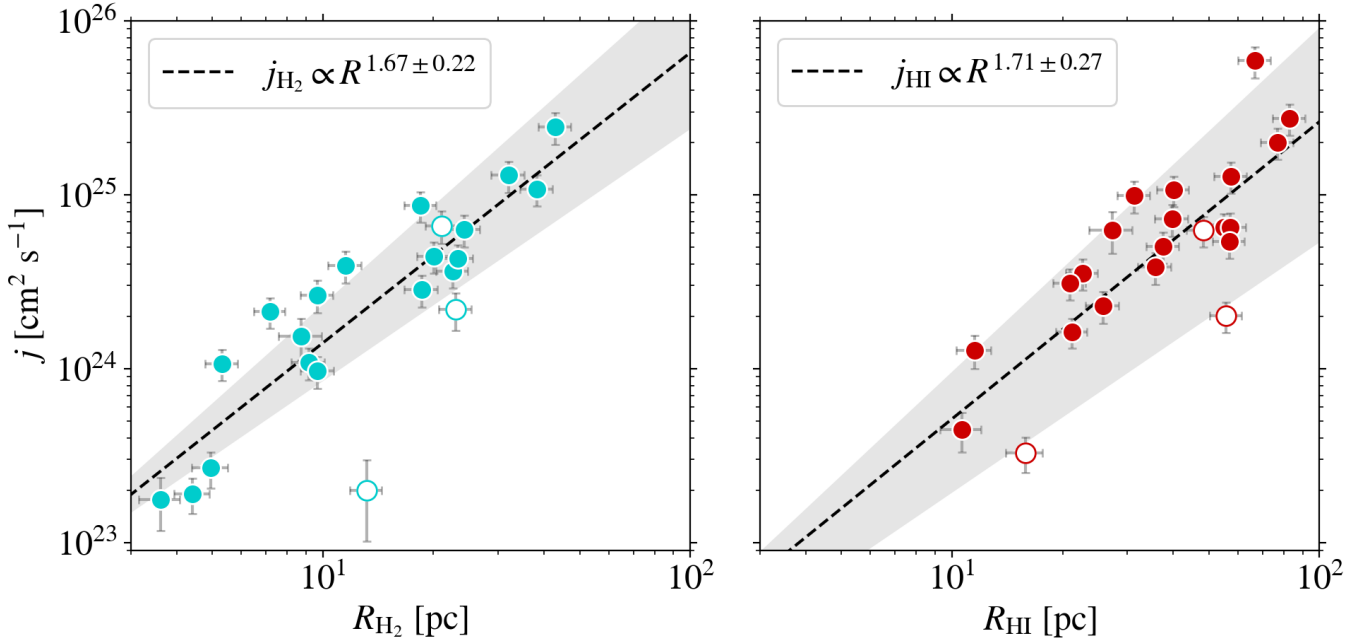


**Figure 9.** The specific angular momentum of molecular clouds (*left*) and their HI envelopes (*right*) as a function of size. The dashed lines are the least-squares fit to the data, and the shaded regions indicate the  $\pm 1\sigma$  error of each fit. The unfilled data points belong to molecular clouds (HI envelopes) with correlation coefficients of  $\leq 0.5$  (0.75).

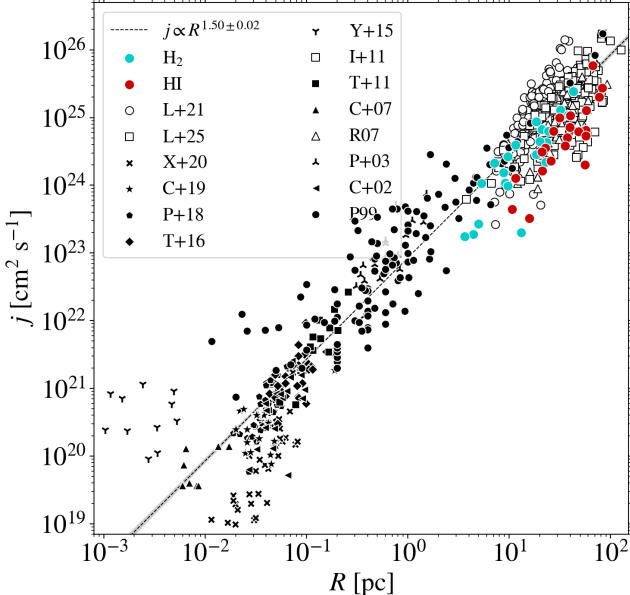


**Figure 10.** Size-Angular Momentum relation of star-forming regions in the Solar Neighborhood. Extragalactic observations are shown with unfilled markers. The magenta line shows the least-squares fit to the combined data; a supersonic turbulent cascade is observed in the size range  $10^{-3} < R < 10^2$  pc.

them as intermediate between the present day molecular cloud and HI envelope. This suggests that the increase from  $j_{\text{init}}$  to  $j_{\text{HI}}$  is caused by the molecular cloud

redistributing angular momentum into the surrounding HI, consistent with IBB's measurements of isolated HI clouds having smaller angular momenta than those associated with molecular clouds.

To estimate the timescale over which the angular momentum of the progenitor system is transported away from the molecular cloud, we assume that the dominant torque for redistributing angular momentum is also responsible for dissipating the rotational energy from the system. By dimensional analysis, the angular momentum redistribution rate can be written as  $\Delta J / \Delta t_{\text{diss}} \approx \Delta E$ . We then express the redistribution timescale  $\Delta t_{\text{diss}}$  in terms of observationally-derived quantities:

$$\Delta t_{\text{diss}} = \frac{J_{\text{HI}}}{E_{\text{HI}}} = \frac{j_{\text{HI}}}{e_{\text{HI}}} \quad (14)$$

Above, we have assumed that total change in angular momentum  $\Delta J$  reduces to  $\Delta J = J_{\text{init}} - J_{\text{H}_2} = J_{\text{HI}}$ , and that the same logic applies to the total change in rotational energy:  $\Delta E = E_{\text{HI}}$ . The specific rotational energy of the HI envelope is given by:

$$e_{\text{HI}} \approx (\Omega R)^2 \quad (15)$$

The redistribution timescales we calculate using Equation 14 are  $\Delta t_{\text{dis}} \in (4, 80)$  Myr<sup>3</sup>, with an overall median

<sup>3</sup> All but Monoceros OB1 have  $\Delta t_{\text{dis}} < 40$  Myr, which has a longer timescale of  $\sim 80$  Myr

of 13 Myr. This is similar to the free-fall time of the HI envelopes ( $\sim 14$  Myr), and twice as long as the average sound crossing time of both populations and the free-fall time of the molecular clouds ( $\sim 6$  Myr). The redistribution timescale is also 5 (15) times shorter than typical molecular cloud (HI envelope) rotational period. This suggests that potential physical mechanisms for redistributing the angular momentum—e.g., magnetic braking, turbulent dissipation, gravitational torques—will have had the opportunity to brake the gas as it contracts, facilitating gravitational collapse.

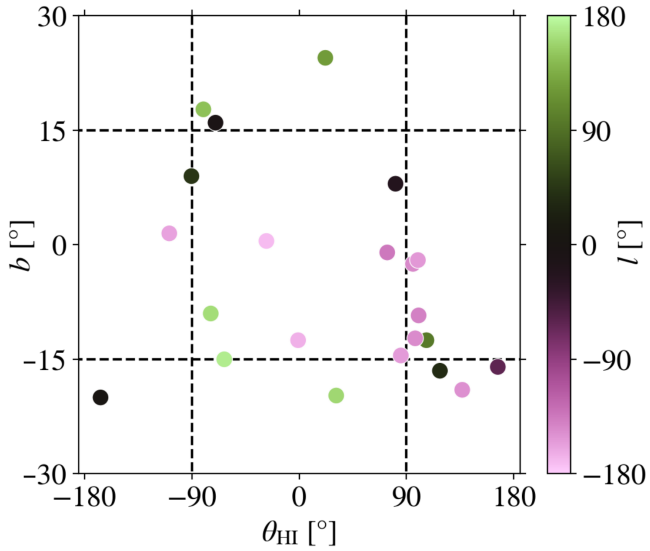


**Figure 11.** Velocity gradient position angles of the HI envelopes, arranged according to Galactic latitude. The color-bar indicates the Galactic longitude coordinate of each envelope.

### 6.2. Overlapping HI envelopes

The axis of large-scale Galaxy rotation lies along  $\phi = 90^\circ$  when viewed from the midplane. About 27% (6) of the molecular clouds, and 3 of the HI envelopes have angular momentum vectors aligned with the Milky Way  $\Delta\phi = |\phi_{\text{Gal}} - \phi_{\text{H}_2}| < 45^\circ$  (Figure 7). On the other hand, three times as many of the HI clouds have  $|\phi| \leq 45^\circ$ . If  $\Omega_{\text{HI}}$  arose due to rotation, this would imply that their rotation planes that are perpendicular to the Galactic plane, which is unexpected given the dynamical coupling of HI clouds to the Galaxy (e.g., Jeffreson et al. 2020), this is unexpected. One would rather expect that  $\phi_{\text{HI}} \sim 90^\circ$ . Further examination shows that 5 of these HI envelopes share similar on-sky coordinates (Figure 11), with the overlap among their velocity fields artificially increasing the occurrence rate of vertical velocity gradients.

Future work can improve upon this by distinguishing between molecular clouds that share a common HI envelope, and those where the overlap is due to chance. The former will require refining our model of angular momentum redistribution to account for the co-evolution of multiple molecular clouds within a shared envelope. For those clouds whose HI envelopes overlap purely due to projection, the velocity fields of the foreground and background systems need to be disentangled. This necessitates characterizing the distribution of emitting material along the line-of-sight, e.g., using dust-derived three-dimensional reconstructions of the Solar Neighborhood such as those by Dharmawardena et al. 2024; Edenhofer et al. 2024; Leike et al. 2020.

## 7. SUMMARY AND CONCLUSIONS

With the aim of investigating the angular momentum in molecular clouds and their associated HI envelopes, we identify atomic gas associated with 22 molecular clouds in the Solar Neighborhood, following Imara & Blitz (2011) and Imara et al. (2011).

- We measure the properties of the molecular clouds and their associated HI envelopes using  $^{12}\text{CO}$  and 21-cm observations. The accumulation radii of the HI envelopes are on average 3 times larger and more massive compared to the molecular cloud with which they are associated (Table 2).
- The velocity field maps (Figure 3) of both populations are fit with planes to derive the large-scale velocity gradients,  $\Omega_{\text{HI}}$  and  $\Omega_{\text{H}_2}$ . The molecular clouds have typical velocity gradients of  $\Omega_{\text{H}_2} \approx 0.1 \text{ km s}^{-1} \text{ pc}^{-1}$ , while the HI have gradients of  $\Omega_{\text{HI}} \approx 0.03 \text{ km s}^{-1}$ . The rotation axes of a molecular clouds and its HI envelopes tend to be unaligned, with separations distributed randomly between  $0^\circ$  and  $180^\circ$  (Figure 4).
- Our results demonstrate that a simple top-down collapse model is insufficient to explain the discrepancy between the angular momenta of molecular clouds and those of the atomic gas in their vicinity. The average specific angular momentum of the HI envelopes is  $j_{\text{HI}} \approx 9.1 \times 10^{24} \text{ cm}^2 \text{ s}^{-1}$ , and is on average 4 times larger than the corresponding  $j_{\text{H}_2}$  (Figure 8). Along with the abundance of systems with large angular separations of molecular cloud and HI rotation axes, our results builds on a growing body of evidence that molecular clouds have systematically smaller, and misaligned, angular momenta than would be expected had they formed via direct collapse from the surrounding HI. This result suggests that angular momentum

redistribution has occurred following the formation of molecular clouds.

- The specific angular momentum of molecular clouds scales with size as  $j_{\text{H}_2} \propto R^{1.67 \pm 0.22}$ , while the HI envelopes follow a steeper relation of  $j_{\text{HI}} \propto R^{1.71 \pm 0.27}$  (Figure 9). Both are consistent with the  $j \propto R^{1.5}$  scaling expected of supersonic turbulence. We also demonstrate that molecular clouds and cores over five orders of magnitude in size follow the  $j \propto R^{1.5}$  scaling of a supersonic turbulent cascade (Figure 10).
- We develop a physical model describing the co-evolution of the angular momenta of the molecular and atomic phases in Section 6.1, and estimate the specific angular momentum of the progenitor HI cloud from which the present-day molecular cloud-HI envelope system formed. We use also this model to derive the timescales on which an-

gular momentum is redistributed from the molecular clouds to their surrounding HI. We find that the redistribution timescales,  $\Delta t_{\text{dis}} \sim 13$  Myr, are within a factor of 2 of the sound crossing time and free-fall time of the clouds.

<sup>1</sup> We are grateful to Eric Koch, John Forbes, Chris McKee, and Karin Sandstrom for insightful discussions that helped to improve this paper. We also thank an anonymous referee for their constructive feedback. We acknowledge support from the Heising–Simons Foundation (grant 2022-3532) for this work.

*Software:* astropy (Astropy Collaboration et al. 2013, 2018, 2022), matplotlib (Developers 2016), pandas (Reback et al. 2022), scipy (Virtanen et al. 2018), numpy (Harris et al. 2020), joblib (The joblib developers 2025)

## REFERENCES

Arroyo-Chávez, G., & Vázquez-Semadeni, E. 2022, ApJ, 925, 78, doi: [10.3847/1538-4357/ac3915](https://doi.org/10.3847/1538-4357/ac3915)

Arroyo-Chavez, G., Vazquez-Semadeni, E., & Wurster, J. 2026, arXiv e-prints, arXiv:2601.11830, doi: [10.48550/arXiv.2601.11830](https://doi.org/10.48550/arXiv.2601.11830)

Astropy Collaboration, Robitaille, T. P., Tollerud, E. J., et al. 2013, A&A, 558, A33, doi: [10.1051/0004-6361/201322068](https://doi.org/10.1051/0004-6361/201322068)

Astropy Collaboration, Price-Whelan, A. M., Sipőcz, B. M., et al. 2018, AJ, 156, 123, doi: [10.3847/1538-3881/aabc4f](https://doi.org/10.3847/1538-3881/aabc4f)

Astropy Collaboration, Price-Whelan, A. M., Lim, P. L., et al. 2022, ApJ, 935, 167, doi: [10.3847/1538-4357/ac7c74](https://doi.org/10.3847/1538-4357/ac7c74)

Blitz, L. 1993, in Protostars and Planets III, ed. E. H. Levy & J. I. Lunine, 125

Braine, J., Hughes, A., Rosolowsky, E., et al. 2020, A&A, 633, A17, doi: [10.1051/0004-6361/201834613](https://doi.org/10.1051/0004-6361/201834613)

Braine, J., Rosolowsky, E., Gratier, P., Corbelli, E., & Schuster, K. F. 2018, A&A, 612, A51, doi: [10.1051/0004-6361/201732405](https://doi.org/10.1051/0004-6361/201732405)

Burkert, A., & Bodenheimer, P. 2000, ApJ, 543, 822, doi: [10.1086/317122](https://doi.org/10.1086/317122)

Caselli, P., Benson, P. J., Myers, P. C., & Tafalla, M. 2002, ApJ, 572, 238, doi: [10.1086/340195](https://doi.org/10.1086/340195)

Chen, C.-Y., & Ostriker, E. C. 2018, ApJ, 865, 34, doi: [10.3847/1538-4357/aad905](https://doi.org/10.3847/1538-4357/aad905)

Chen, C.-Y., Storm, S., Li, Z.-Y., et al. 2019a, MNRAS, 490, 527, doi: [10.1093/mnras/stz2633](https://doi.org/10.1093/mnras/stz2633)

Chen, H. H.-H., Pineda, J. E., Offner, S. S. R., et al. 2019b, ApJ, 886, 119, doi: [10.3847/1538-4357/ab4ce9](https://doi.org/10.3847/1538-4357/ab4ce9)

Chen, X., Launhardt, R., & Henning, T. 2007, ApJ, 669, 1058, doi: [10.1086/521868](https://doi.org/10.1086/521868)

Dame, T. M. 2011, arXiv e-prints, arXiv:1101.1499, doi: [10.48550/arXiv.1101.1499](https://doi.org/10.48550/arXiv.1101.1499)

Dame, T. M., Hartmann, D., & Thaddeus, P. 2001, ApJ, 547, 792, doi: [10.1086/318388](https://doi.org/10.1086/318388)

Developers, M. 2016, doi: [10.5281/zenodo.61948](https://doi.org/10.5281/zenodo.61948)

Dharmawardena, T. E., Bailer-Jones, C. A. L., Fouesneau, M., et al. 2024, MNRAS, 532, 3480, doi: [10.1093/mnras/stae1474](https://doi.org/10.1093/mnras/stae1474)

Edenhofer, G., Zucker, C., Frank, P., et al. 2024, A&A, 685, A82, doi: [10.1051/0004-6361/202347628](https://doi.org/10.1051/0004-6361/202347628)

Goodman, A. A., Benson, P. J., Fuller, G. A., & Myers, P. C. 1993, ApJ, 406, 528, doi: [10.1086/172465](https://doi.org/10.1086/172465)

Harris, C. R., Millman, K. J., van der Walt, S. J., et al. 2020, Nature, 585, 357, doi: [10.1038/s41586-020-2649-2](https://doi.org/10.1038/s41586-020-2649-2)

HI4PI Collaboration, Ben Bekhti, N., Flöer, L., et al. 2016a, A&A, 594, A116, doi: [10.1051/0004-6361/201629178](https://doi.org/10.1051/0004-6361/201629178)

HI4PI Collaboration, Ben Bekhti, N., Floer, L., et al. 2016b, HI4PI spectra and column density maps, Centre de Donnees Strasbourg (CDS), doi: [10.26093/CDS/VIZIER.35940116](https://doi.org/10.26093/CDS/VIZIER.35940116)

Imara, N., Bigiel, F., & Blitz, L. 2011, ApJ, 732, 79, doi: [10.1088/0004-637X/732/2/79](https://doi.org/10.1088/0004-637X/732/2/79)

Imara, N., & Blitz, L. 2011, ApJ, 732, 78, doi: [10.1088/0004-637X/732/2/78](https://doi.org/10.1088/0004-637X/732/2/78)

Imara, N., & Burkhardt, B. 2016, ApJ, 829, 102, doi: [10.3847/0004-637X/829/2/102](https://doi.org/10.3847/0004-637X/829/2/102)

Jeffreson, S. M. R., Kruijssen, J. M. D., Keller, B. W., Chevance, M., & Glover, S. C. O. 2020, Monthly Notices of the Royal Astronomical Society, 498, 385–429, doi: [10.1093/mnras/staa2127](https://doi.org/10.1093/mnras/staa2127)

Kalberla, P. M. W., Burton, W. B., Hartmann, D., et al. 2005, A&A, 440, 775, doi: [10.1051/0004-6361:20041864](https://doi.org/10.1051/0004-6361:20041864)

Krumholz, M. R., McKee, C. F., & Tumlinson, J. 2009, ApJ, 693, 216, doi: [10.1088/0004-637X/693/1/216](https://doi.org/10.1088/0004-637X/693/1/216)

Kutner, M. L., Tucker, K. D., Chin, G., & Thaddeus, P. 1977, ApJ, 215, 521, doi: [10.1086/155384](https://doi.org/10.1086/155384)

Larson, R. B. 1981, MNRAS, 194, 809, doi: [10.1093/mnras/194.4.809](https://doi.org/10.1093/mnras/194.4.809)

—. 1984, MNRAS, 206, 197, doi: [10.1093/mnras/206.1.197](https://doi.org/10.1093/mnras/206.1.197)

Leike, R. H., Glatzle, M., & Enßlin, T. A. 2020, A&A, 639, A138, doi: [10.1051/0004-6361/202038169](https://doi.org/10.1051/0004-6361/202038169)

Lewis, J. A., Lada, C. J., & Dame, T. M. 2022, ApJ, 931, 9, doi: [10.3847/1538-4357/ac5d58](https://doi.org/10.3847/1538-4357/ac5d58)

Liu, L., Bureau, M., Blitz, L., et al. 2021, MNRAS, 505, 4048, doi: [10.1093/mnras/stab1537](https://doi.org/10.1093/mnras/stab1537)

Machida, M. N., Tomisaka, K., Matsumoto, T., & Inutsuka, S.-i. 2008, ApJ, 677, 327, doi: [10.1086/529133](https://doi.org/10.1086/529133)

Misugi, Y., Inutsuka, S.-i., Arzoumanian, D., & Tsukamoto, Y. 2024, ApJ, 963, 106, doi: [10.3847/1538-4357/ad1990](https://doi.org/10.3847/1538-4357/ad1990)

Mouschovias, T. C., & Paleologou, E. V. 1979, ApJ, 230, 204, doi: [10.1086/157077](https://doi.org/10.1086/157077)

Pandhi, A., Friesen, R. K., Fissel, L., et al. 2023, MNRAS, 525, 364, doi: [10.1093/mnras/stad2283](https://doi.org/10.1093/mnras/stad2283)

Park, G., Koo, B.-C., Kim, K.-T., & Elmegreen, B. 2023, ApJ, 955, 59, doi: [10.3847/1538-4357/acebda](https://doi.org/10.3847/1538-4357/acebda)

Phillips, J. P. 1998

—. 1999, A&AS, 134, 241, doi: [10.1051/aas:1999137](https://doi.org/10.1051/aas:1999137)

Pirogov, L., Zinchenko, I., Caselli, P., Johansson, L. E. B., & Myers, P. C. 2003, A&A, 405, 639, doi: [10.1051/0004-6361:20030659](https://doi.org/10.1051/0004-6361:20030659)

Punanova, A., Caselli, P., Pineda, J. E., et al. 2018, A&A, 617, A27, doi: [10.1051/0004-6361/201731159](https://doi.org/10.1051/0004-6361/201731159)

Reback, J., Jbrockmendel, McKinney, W., et al. 2022, doi: [10.5281/zenodo.6053272](https://doi.org/10.5281/zenodo.6053272)

Rosolowsky, E. 2007, ApJ, 654, 240, doi: [10.1086/509249](https://doi.org/10.1086/509249)

Rosolowsky, E., Engargiola, G., Plambeck, R., & Blitz, L. 2003, ApJ, 599, 258, doi: [10.1086/379166](https://doi.org/10.1086/379166)

Saha, P., Roy, N., & Bhattacharya, M. 2018, MNRAS, 480, L126, doi: [10.1093/mnrasl/sly139](https://doi.org/10.1093/mnrasl/sly139)

Shen, Y.-F., Xu, Y., Wang, Y.-B., et al. 2025, ApJ, 988, 125, doi: [10.3847/1538-4357/ade399](https://doi.org/10.3847/1538-4357/ade399)

Stanimirović, S., Murray, C. E., Lee, M.-Y., Heiles, C., & Miller, J. 2014, ApJ, 793, 132, doi: [10.1088/0004-637X/793/2/132](https://doi.org/10.1088/0004-637X/793/2/132)

Sternberg, A., Gurman, A., & Bialy, S. 2021, ApJ, 920, 83, doi: [10.3847/1538-4357/ac167b](https://doi.org/10.3847/1538-4357/ac167b)

Sun, S., Wang, K., Liu, X., & Xu, F. 2024, ApJL, 973, L27, doi: [10.3847/2041-8213/ad77ce](https://doi.org/10.3847/2041-8213/ad77ce)

Tatematsu, K., Ohashi, S., Sanhueza, P., et al. 2016, PASJ, 68, 24, doi: [10.1093/pasj/psw002](https://doi.org/10.1093/pasj/psw002)

The joblib developers. 2025, doi: [10.5281/zenodo.15496554](https://doi.org/10.5281/zenodo.15496554)

Tobin, J. J., Hartmann, L., Chiang, H.-F., et al. 2011, ApJ, 740, 45, doi: [10.1088/0004-637X/740/1/45](https://doi.org/10.1088/0004-637X/740/1/45)

Vázquez-Semadeni, E., Palau, A., Gómez, G. C., et al. 2024, arXiv e-prints, arXiv:2408.10406, doi: [10.48550/arXiv.2408.10406](https://doi.org/10.48550/arXiv.2408.10406)

Virtanen, P., Gommers, R., Burovski, E., et al. 2018, doi: [10.5281/zenodo.1218715](https://doi.org/10.5281/zenodo.1218715)

Wolfire, M. G., McKee, C. F., Hollenbach, D., & Tielens, A. G. G. M. 2003, ApJ, 587, 278, doi: [10.1086/368016](https://doi.org/10.1086/368016)

Xu, X., Li, D., Dai, Y. S., Goldsmith, P. F., & Fuller, G. A. 2020, The Astrophysical Journal, 898, 122, doi: [10.3847/1538-4357/ab9a45](https://doi.org/10.3847/1538-4357/ab9a45)

Yen, H.-W., Koch, P. M., Takakuwa, S., et al. 2015, ApJ, 799, 193, doi: [10.1088/0004-637X/799/2/193](https://doi.org/10.1088/0004-637X/799/2/193)

Yen, H.-W., & Lee, Y.-N. 2024, ApJL, 972, L27, doi: [10.3847/2041-8213/ad7263](https://doi.org/10.3847/2041-8213/ad7263)

Zucker, C., Speagle, J. S., Schlafly, E. F., et al. 2019, ApJ, 879, 125, doi: [10.3847/1538-4357/ab2388](https://doi.org/10.3847/1538-4357/ab2388)

## APPENDIX

## A. VELOCITY SPECTRA

We calculate the one-dimensional velocity spectrum of each molecular cloud by taking the average brightness temperature of  $^{12}\text{CO}$  emission within a subcube, extracted from Dame et al. (2001) according to the latitude and longitude bounds given in Table 1. We sum emission in the range  $v_{\text{H}_2} \in \pm 50 \text{ km s}^{-1}$ . The HI envelope spectra are calculated from subcubes extracted from HI4PI Collaboration et al. (2016b). We define the center of the HI envelope to coincide with the center of the molecular cloud, and its latitude and longitude bounds define a square of side length of  $2R_{\text{HI}}$ . To convert from linear to angular units, we assume that the HI envelope is located at the same distance as the molecular cloud with which it is associated. We fit the 21-cm spectrum with a Gaussian1D model from `astropy.modeling`, using the Trust Region Reflective algorithm in `astropy.fitting` to obtain the linecenter  $v_{\text{HI}}$  and linewidth  $\sigma_{\text{HI}}$ .

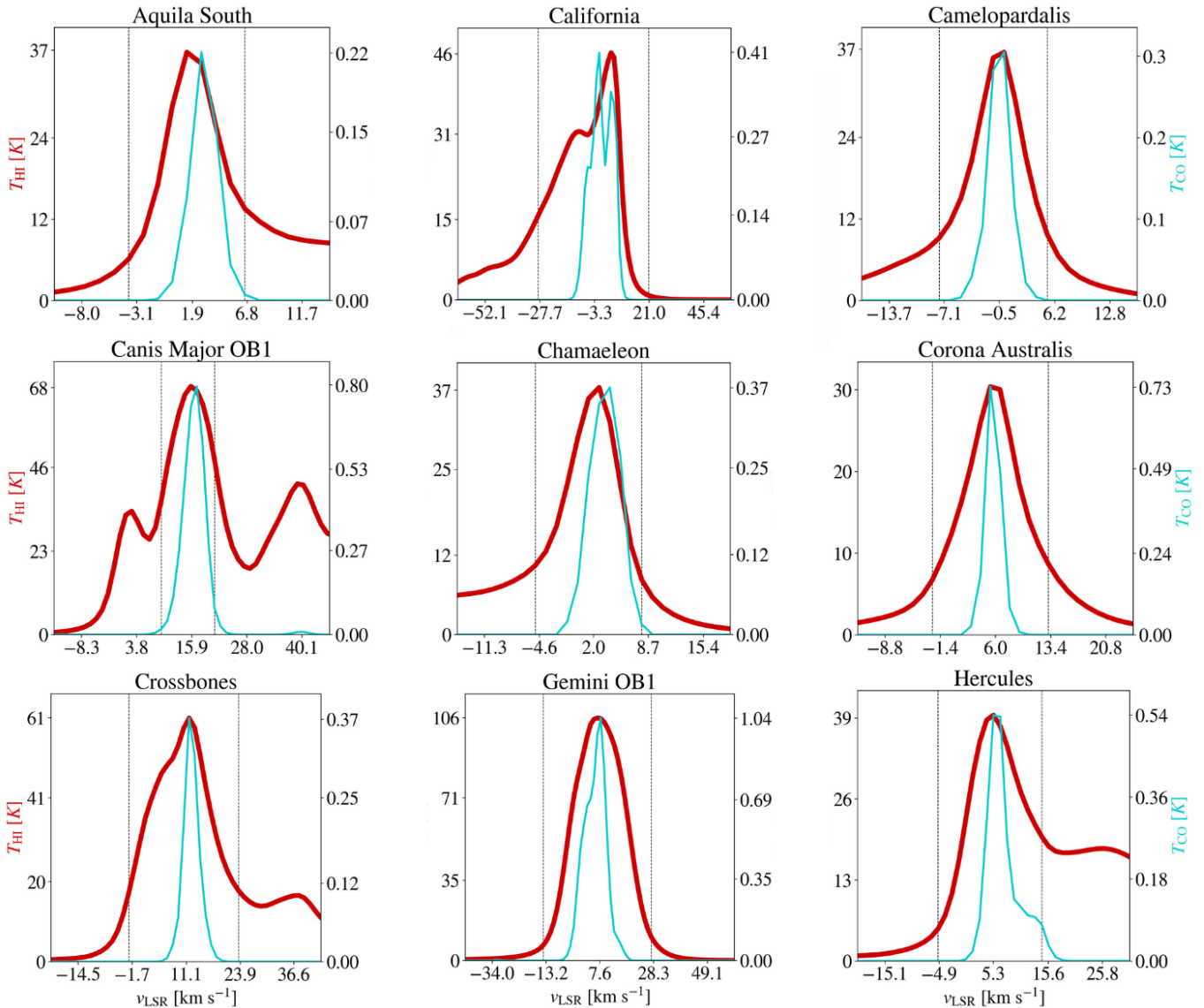


**Figure A.1.** Velocity spectra of the molecular clouds (blue) and their associated HI envelopes (red). The vertical lines indicate velocity bounds used to define the HI envelope.

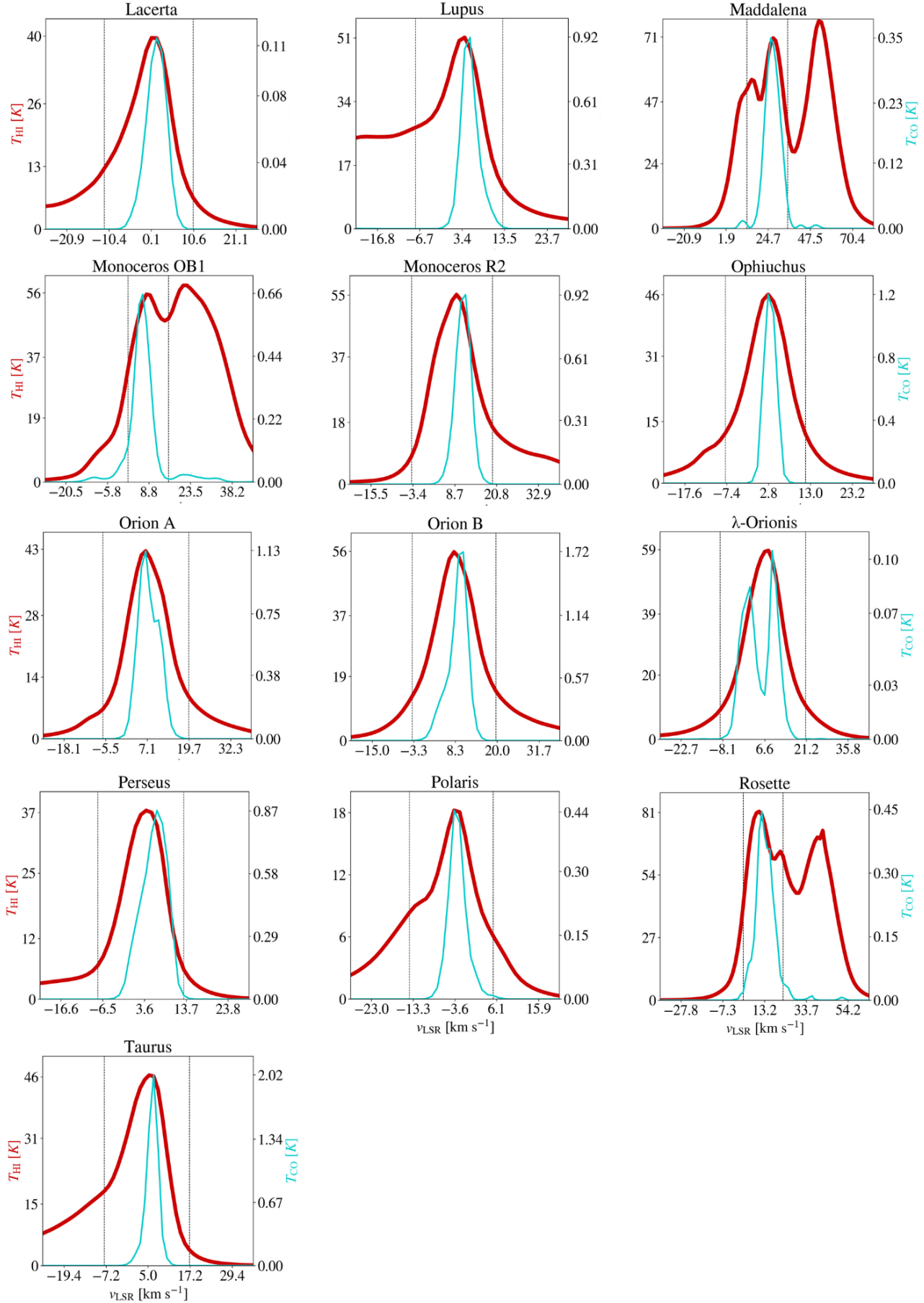
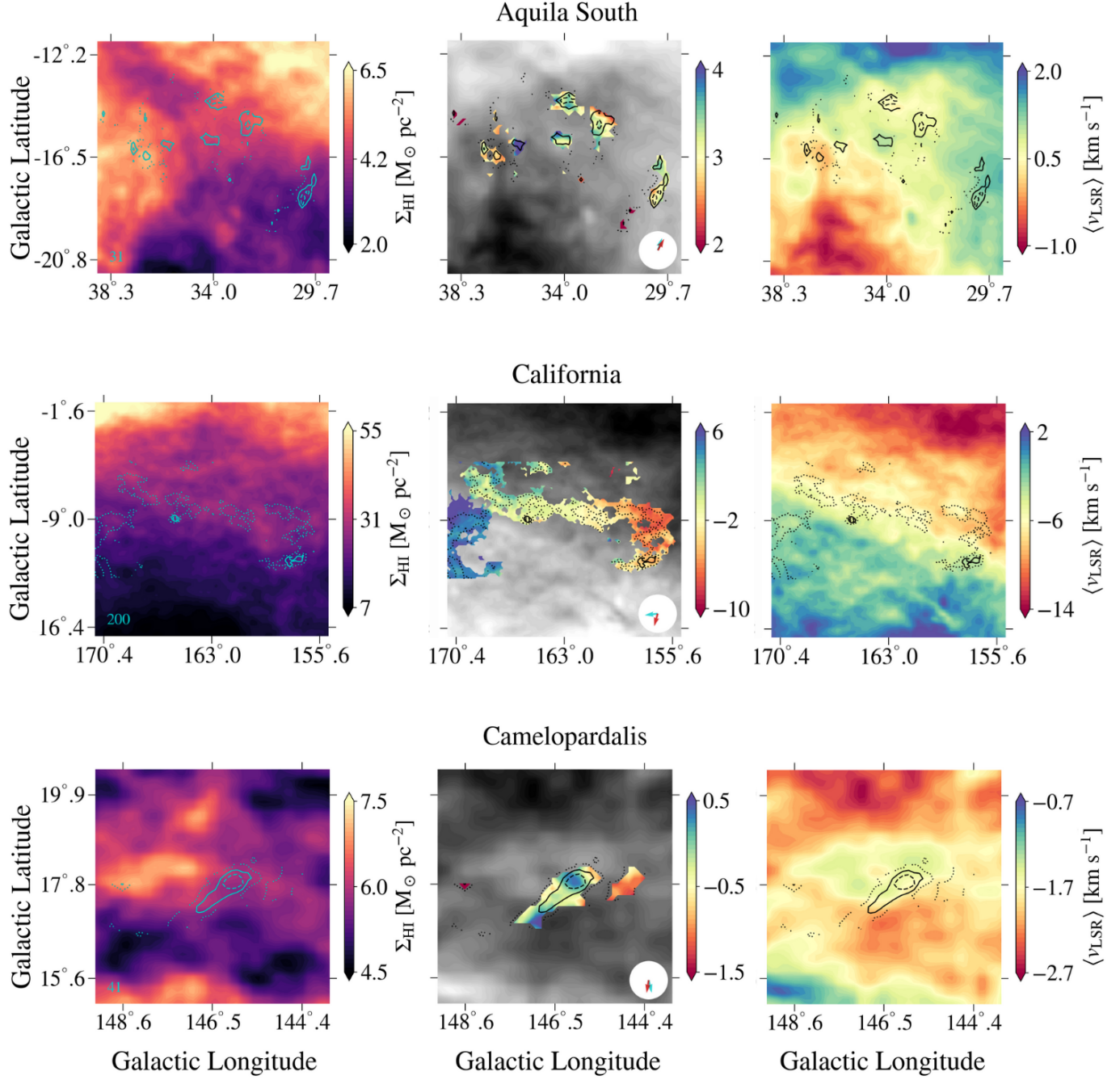


Figure A.2. Same as Figure A.1

## B. SURFACE DENSITY AND VELOCITY FIELD MAPS

The surface density maps of the HI envelopes are presented below, along with the velocity field maps of both populations. In all the systems, the peak H<sub>2</sub> surface density is much larger than the  $\Sigma_{\text{HI,peak}}$ . For the Orion A and B clouds, the molecular gas is  $> 20 \times$  denser than the surrounding HI.



**Figure B.1.** Surface density map of the HI envelope around the Perseus molecular cloud (black outline). The overlaid blue contours are at  $(0.25, 0.5, 0.75) \times \Sigma_{\text{H}_2,\text{max}}$ , which is indicated in lower left corner. *Middle:* Velocity field maps of the Perseus molecular cloud and (*right*) HI envelope, derived from the first moments of <sup>12</sup>CO and 21-cm emission at each pixel. The blue (red) arrow in the lower right corner of the middle panel indicates the velocity gradient direction  $\theta_{\text{H}_2}$  ( $\theta_{\text{HI}}$ ).

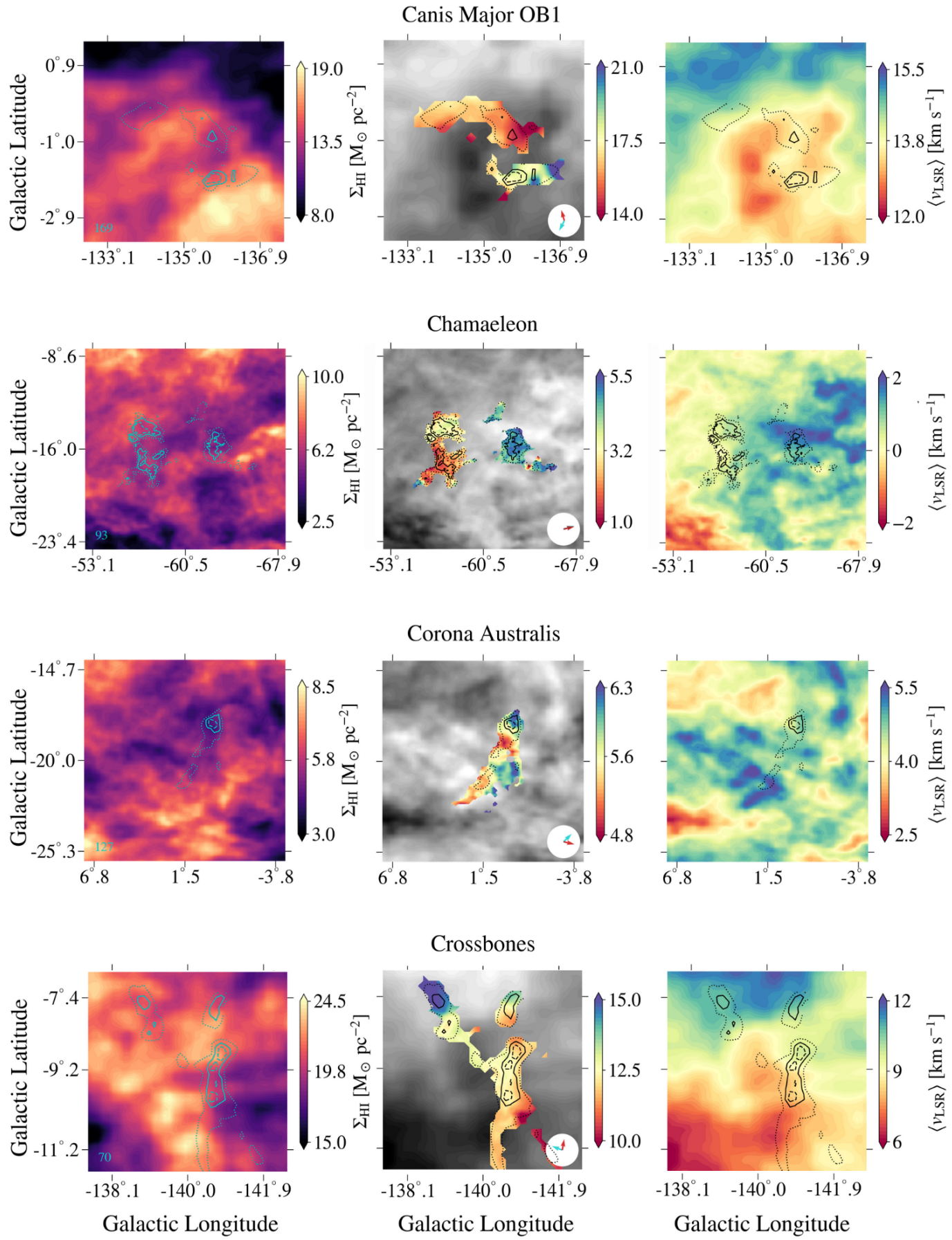


Figure B.2. Same as Figure B.1

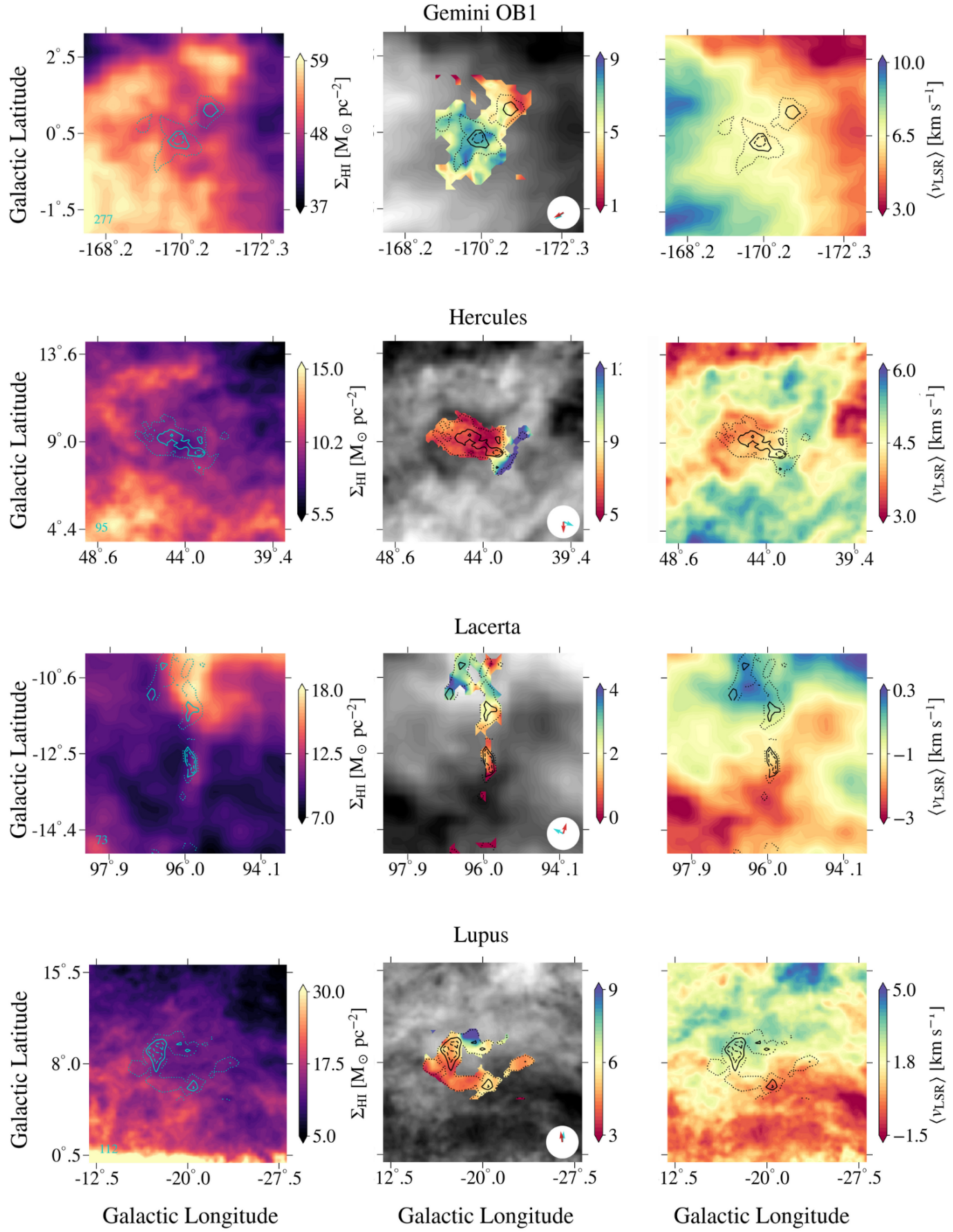


Figure B.3. Same as Figure B.1

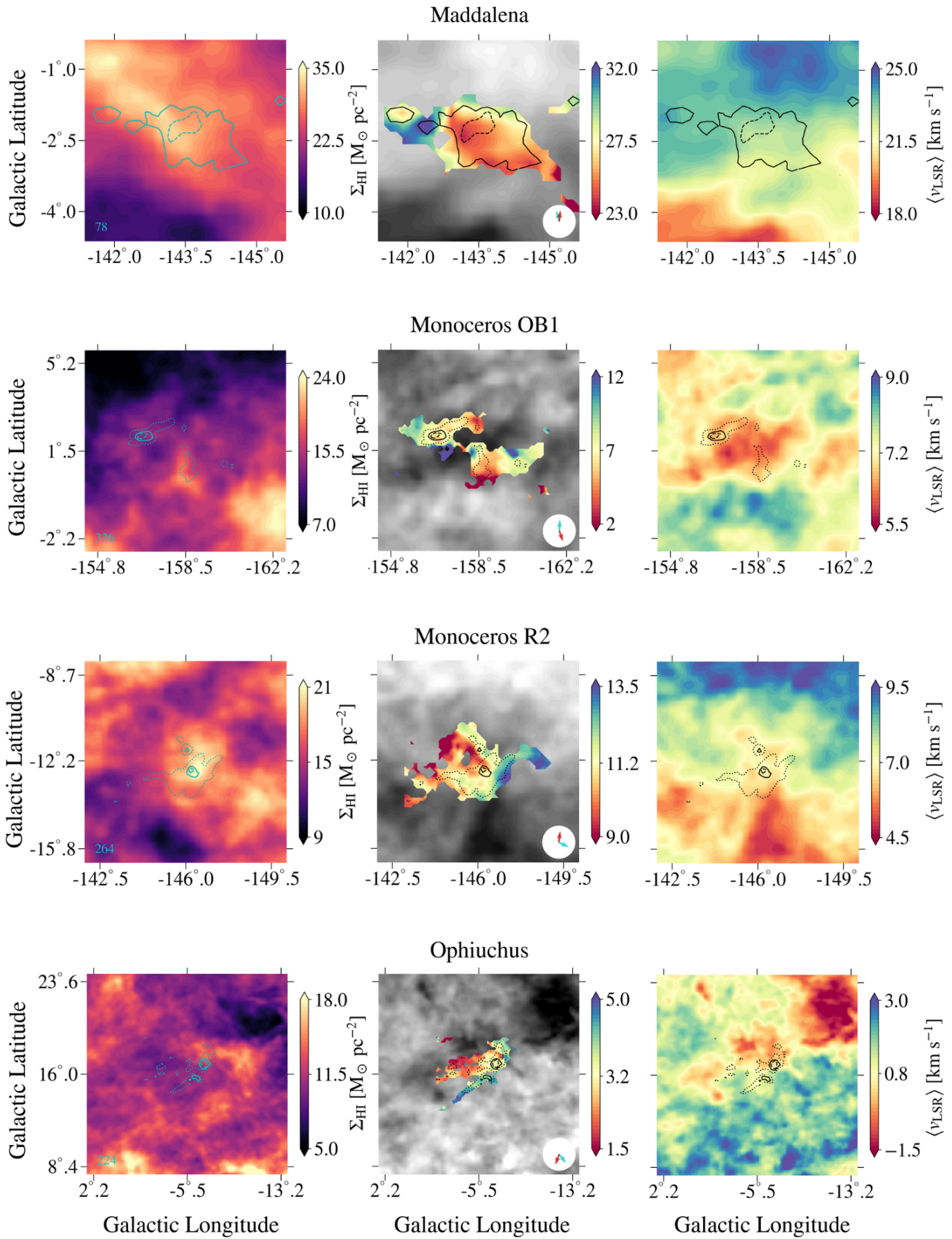


Figure B.4. Same as Figure B.1

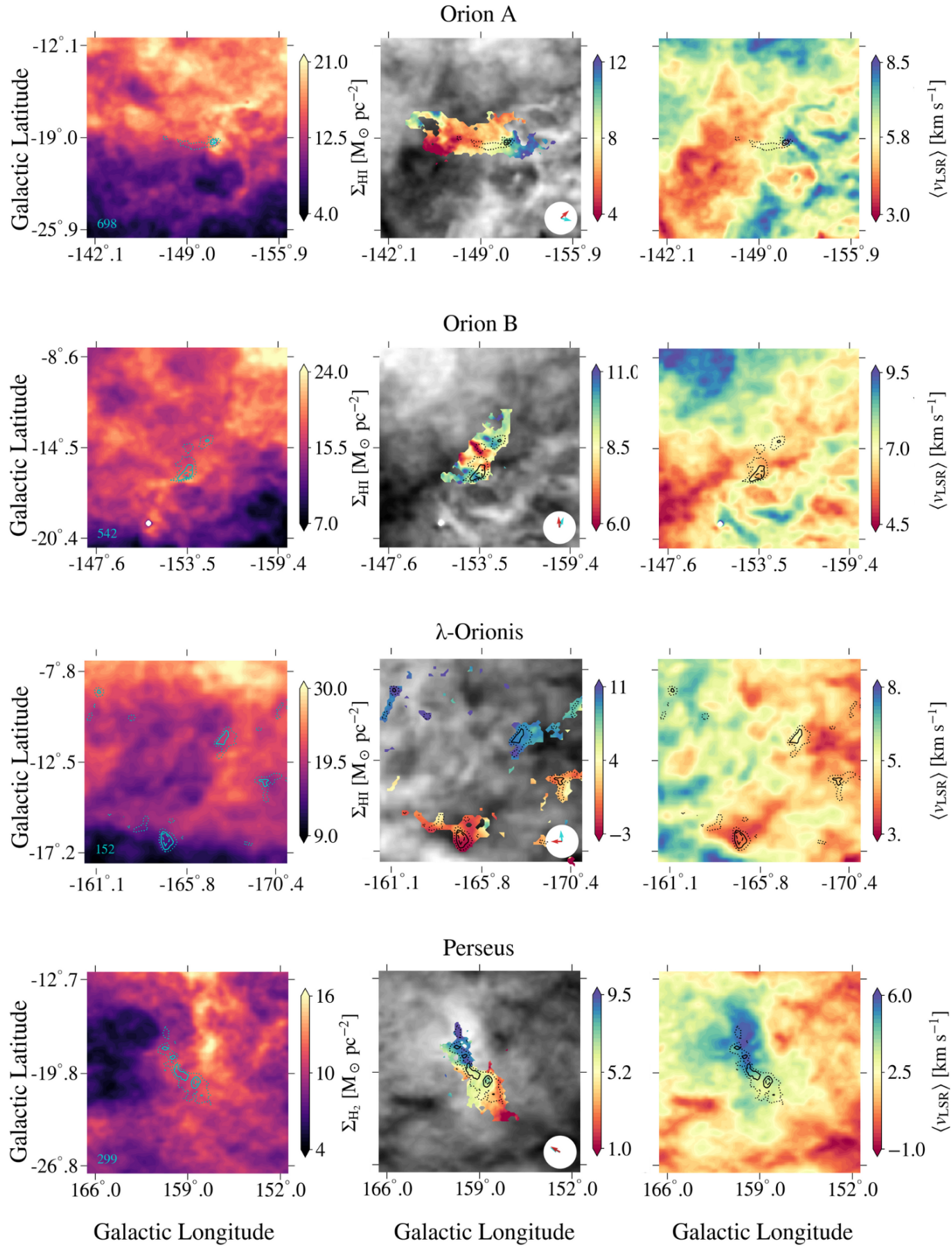
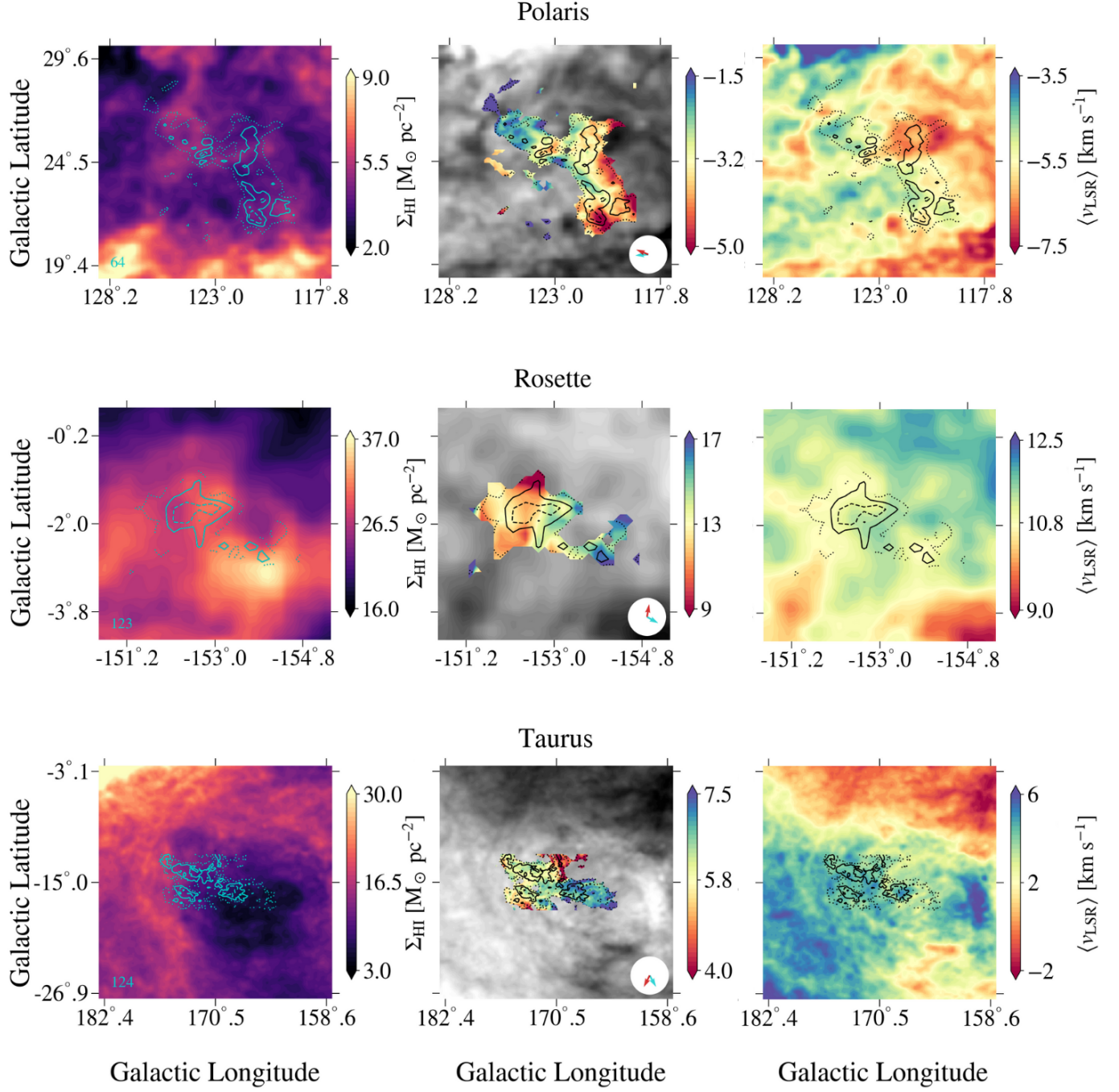


Figure B.5. Same as Figure B.1



**Figure B.6.** Same as Figure B.1

### C. VELOCITY PROFILES

Velocity profiles used to determine the goodness of fit of a plane (Equation 6) for representing the velocity field maps of the molecular clouds and HI envelopes (Appendix B). We use `scipy.optimize.curve_fit` to calculate the least-squares fit, using the inverse second moment maps (available upon request) as weights.

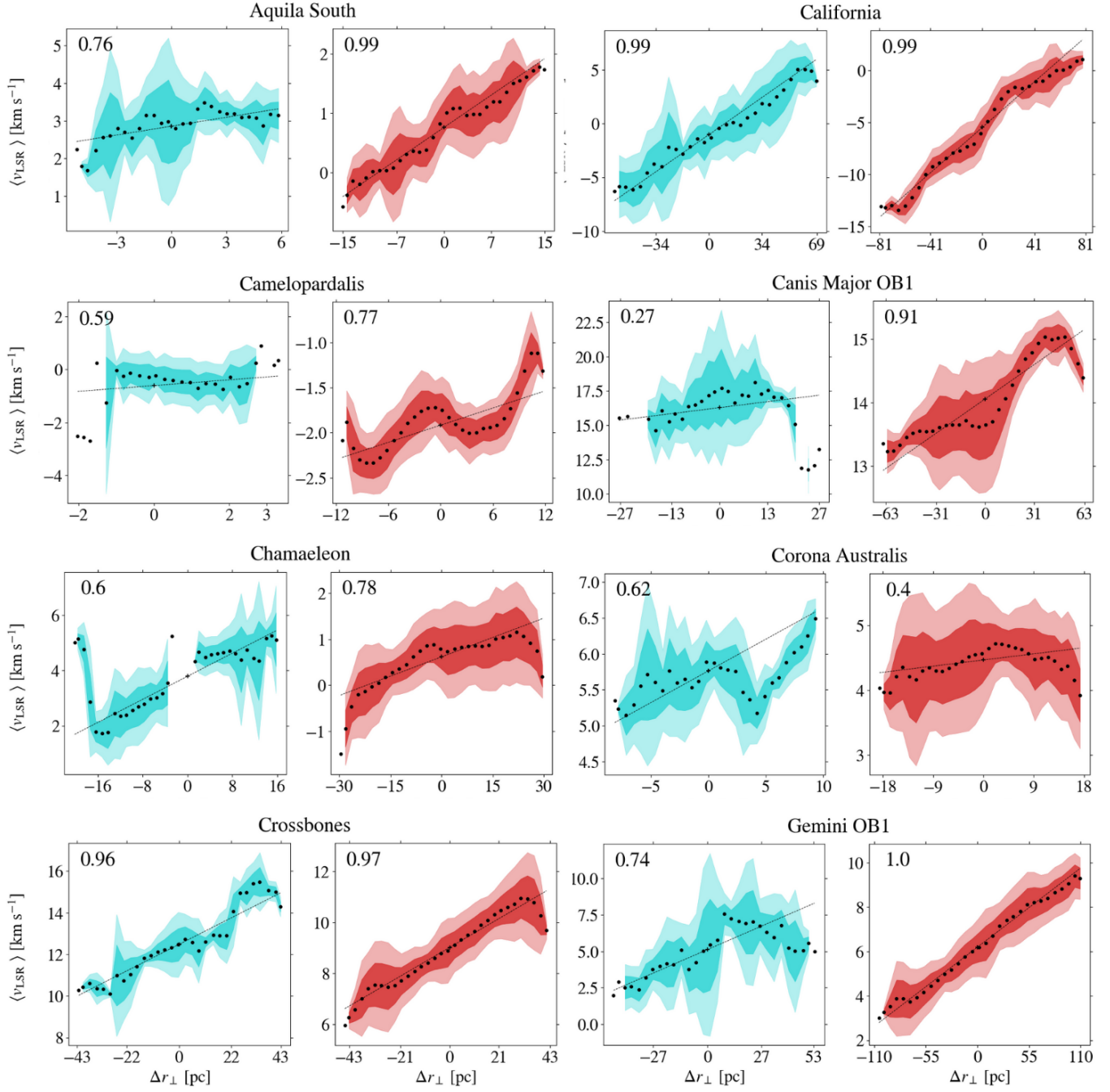


**Figure C.1.** Intensity-weighted velocity centroid,  $\langle v_{\text{LSR}} \rangle$ , as a function of the perpendicular displacement,  $r_{\perp}$ , from the rotation axis of the **each** molecular cloud (*left*) and its HI envelope (*right*). The dashed lines indicate the planar model, and the shaded regions show the  $\pm 1\sigma$  and  $\pm 2\sigma$  scatter of the velocity field map at each radial bin. The Pearson correlation coefficient of the velocity profile is in the upper left corner.

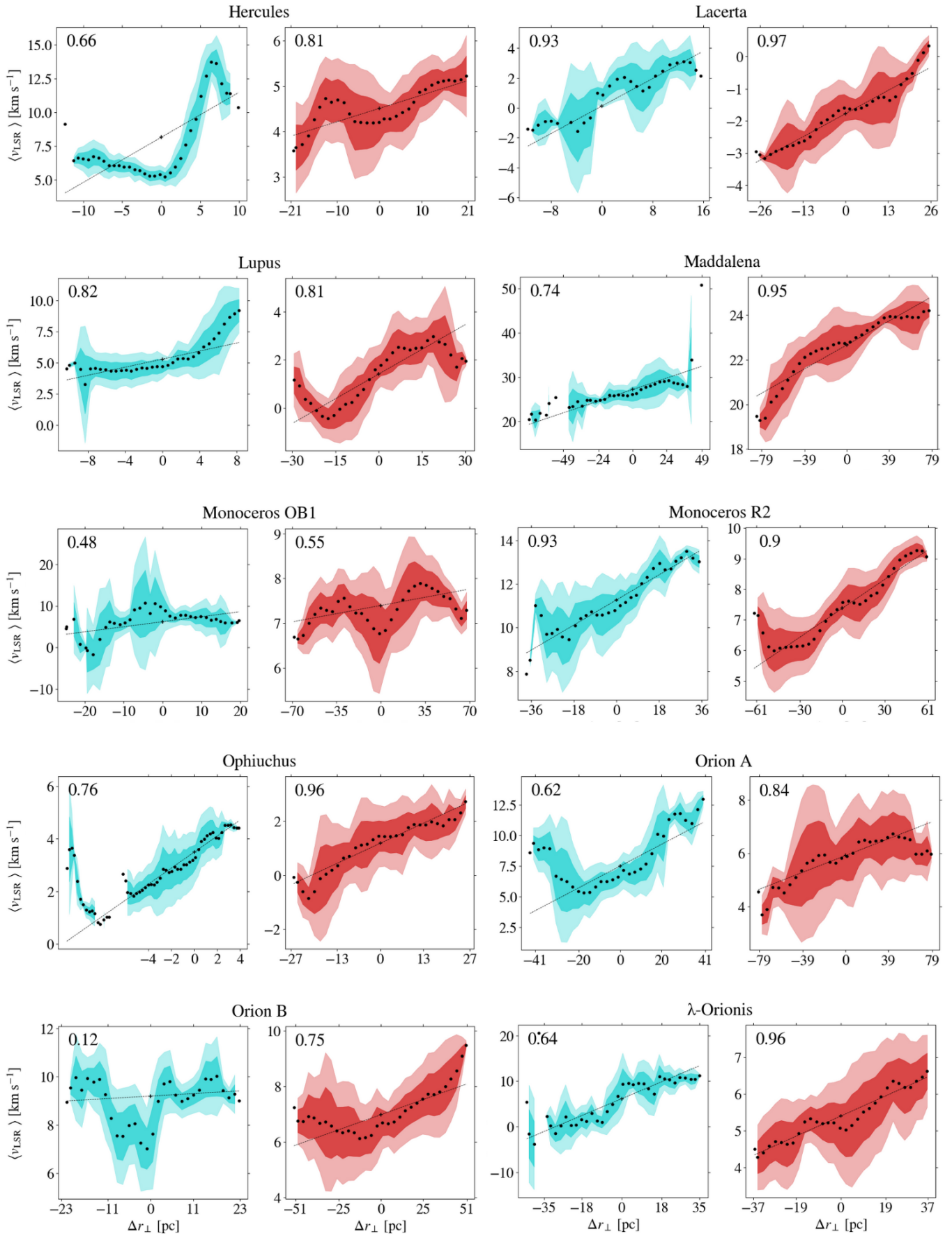
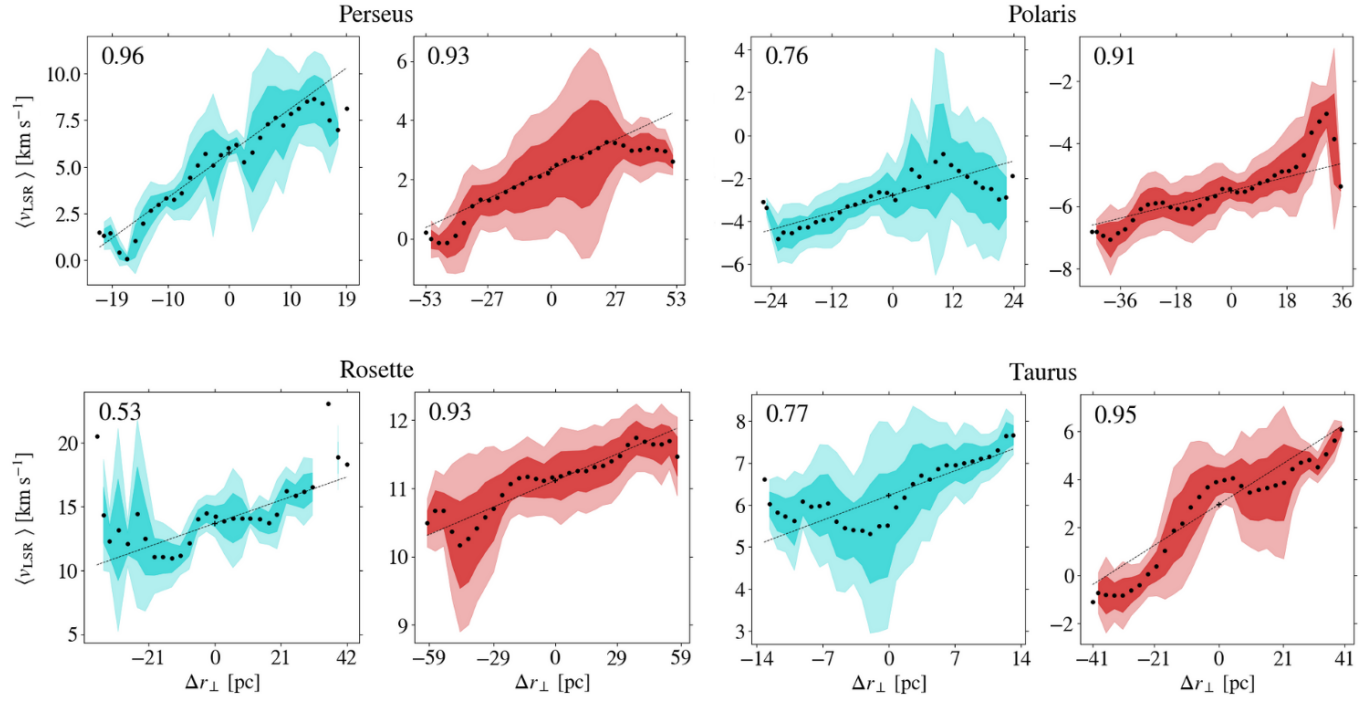


Figure C.2. Same as Figure C.1



**Figure C.3.** Same as Figure C.1